Guy Carpenter Asia-Pacific Climate Impact Centre

Annual Report 2010

GCACIC
Guy Carpenter Asia-Pacific Climate Impact Centre
City University of Hong Kong

香港城市大學
City University of Hong Kong

Executive Summary

This is the second annual report issued by the Guy Carpenter Asia-Pacific Climate Impact Centre and covers the activities of the Centre in 2010. During the year, members of the Centre continued to work on climate problems in the Asia-Pacific region, which includes tropical cyclones, monsoons (both summer and winter), air pollution effects, general climate studies as well as paleoclimatology. As in the past, individual projects that were carried out by individual members of the Centre are briefly described in this report.

Looking ahead, we expect to continue our research in these various areas, with the dual objectives of both an increased understanding of the phenomenon and development of prediction tools to provide a better assessment of the possible climate impacts of these phenomena.

Contents

I. Introduction

This is the second annual report issued by the Guy Carpenter Asia-Pacific Climate Impact Centre and covers the activities of the Centre in 2010. During the year, members of the Centre continued to work on climate problems in the Asia-Pacific region, which includes tropical cyclones, monsoons (both summer and winter), air pollution effects, general climate studies as well as paleoclimatology. We were fortunate to have Professor Wyss Yim with us during the year to lead the work on paleoclimatology, some of which have led to an increased awareness of the teleconnection between volcanic activity and rainfall. This year, with the continued donation from Guy Carpenter and support from the University, we were able to purchase a new PC cluster with 144 nodes, which significantly enhanced our computational capability such that we can now run a general circulation model as well as a regional climate model with a reasonable turn-around time.

As in the past, individual projects that were carried out by individual members of the Centre are briefly described in this report. Details of each project can be found in the list of publications. A copy of each of the publications is included in the CD attached to the report and is also available online at http://www.cityu.edu.hk/gcacic/publications.htm.

II. Research Projects

A. Tropical Cyclones

1. Tropical Cyclone Variability/Predictions in Different Regions in Asia/Pacific

South China

(PI: Johnny CHAN)

This study describes an improved statistical scheme for predicting the annual number of tropical cyclones (TCs) making landfall on the coast of South China using data from 1965 to 2005.

Based on the factors affecting TC behaviour inside the South China Sea (SCS), those responsible for TCs making landfall are identified for developing a scheme to predict the annual number of tropical cyclones (TCs) making landfall on the coast of South China. Equations are then developed using the coefficients of empirical orthogonal functions of these factors to predict, in April, the number of these TCs in the early (May to August) and late (September to December) seasons, and in June, the number in the period between July to December. Compared to previous studies, the new scheme achieves a forecast skill of 51% over climatology, or about 11% higher than the scheme by Liu and Chan (2003), when predicting landfalling TC for the whole season, and seems to be able to capture the decrease in their number in the recent years. Analyses of the flow patterns suggest that the conditions inside the SCS are apparently the major factor affecting the number of landfalling TCs. In years in which this number is above normal, conditions inside the SCS are favourable for TC genesis, and vice versa. The strength of the 500-hPa subtropical high also seems to be a factor in determining whether TCs from the WNP could enter the SCS and make landfall. Scatterplots of the predicted versus observed number of TCs are shown in Figure 1. Details can be found in Goh and Chan (2010).

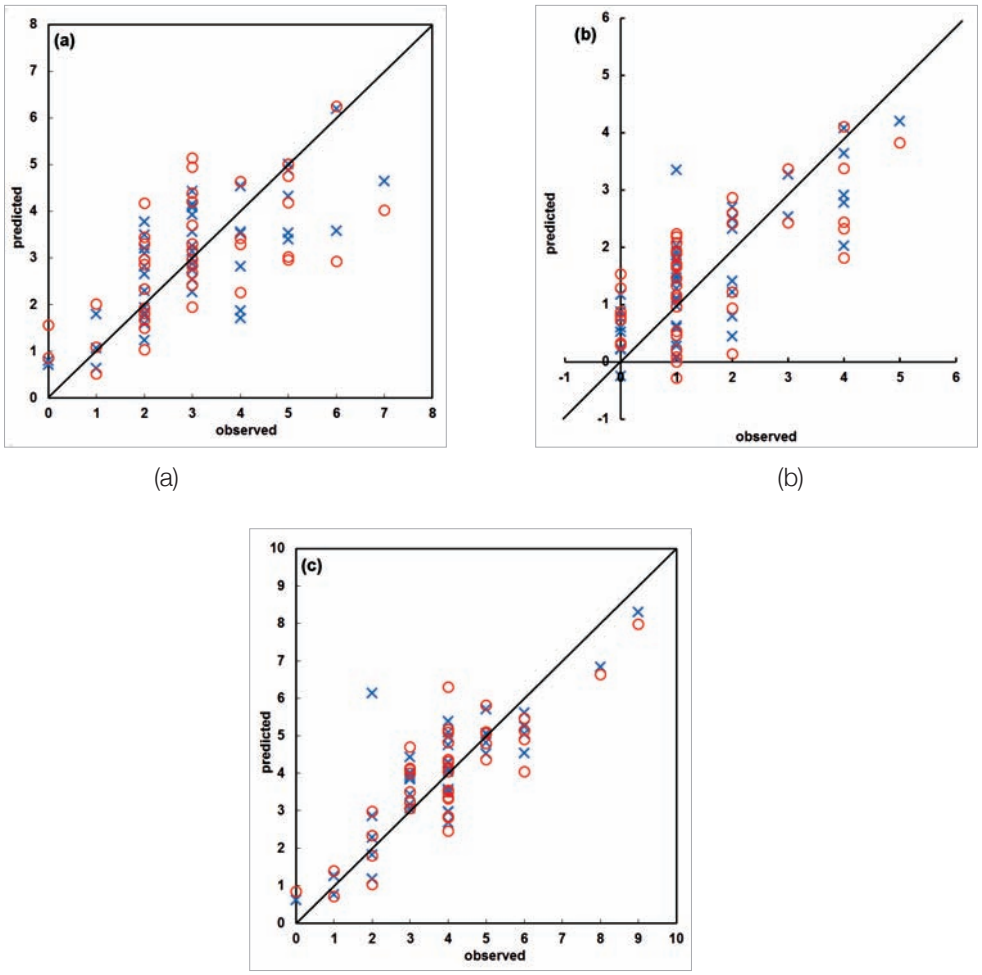

(a) (b) (c)

Figure 1. Scatterplots of calculated versus observed number of landfalling TCs over South China for the April prediction for the (a) early (May to August), (b) late (September to December), and (c) July-December seasons. Crosses indicate values calculated from the prediction equation, while circles are cross-validation values. The thick diagonal straight line is the 45° line indicating perfect prediction.

Korea-Japan
(PI: Johnny CHAN)

This study investigates the factors affecting the annual number of tropical cyclones (TCs) passing within 100 km of the coast of Korea and Japan (KJ), based on which a prediction scheme is also developed for the number of TCs that affect this region.

Factors affecting the annual number of tropical cyclones (TCs) passing within 100 km of the coast of Korea and Japan (KJ) between 1965 and 2005 are identified. Using a training set consisting of the coefficients of empirical orthogonal functions of these factors, equations are derived to predict the annual number of these TCs over the whole season in April, and to update this prediction for the July to November (JN) season in June. Results show that the El Niño-Southern Oscillation (ENSO) plays a key role in determining the behaviour of TCs affecting KJ, with more TCs affecting the region during El Niño and less during La Niña. This difference can be attributed to ENSO modifying the flow patterns, which in turn affects TC behaviour. The prediction equations suggest that the 500-hPa geopotential height is more important in determining the number of TCs affecting KJ in the whole season, while both the 850-hPa geopotential height and 850-hPa vorticity play a role in the JN season. Both prediction schemes are able to produce acceptable results, with forecast skills of 42.3% and 33.3% over climatology for the whole and JN seasons

respectively. The predicted TC number for 2006, 2007 and 2008 are also mostly accurate to within one standard deviation of the observed number. Scatterplots of the predicted versus observed number of TCs are shown in Figure 2. Details can be found in Goh and Chan (2011).

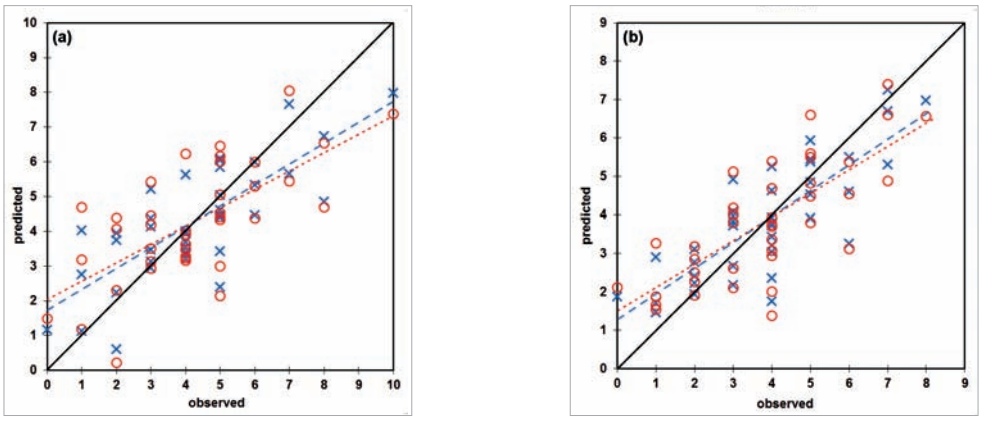

(a) (b)

Figure 2. Scatterplots of calculated versus observed number of TCs affecting the Korea-Japan region for the (a) whole and (b) July-November seasons. Crosses and dashed line indicate values calculated from the prediction equation and their regression line, while circles and dotted line are cross-validated values and their regression line. The thick diagonal straight line is the 45° line indicating perfect prediction.

North Indian Ocean
(PI: Johnny CHAN)

This study examines the interannual variations of tropical cyclone (TC) activity over the North Indian Ocean during 1983-2008. Results show a strong dependence of TC activity over the Bay of Bengal on the El Niño/ Southern Oscillation.

An examination of the interannual variations of tropical cyclone (TC) activity over the North Indian Ocean during 1983-2008 has been carried out in this study. The results suggest that instead of local sea surface temperatures, such variations, at least over the Bay of Bengal (BB) during October-November-December (OND), can be attributed to similar variations in the atmospheric flow patterns and moist static energy that are apparently forced largely by the El Niño/Southern Oscillation (ENSO). In an El Niño year, conditions for TC genesis and development, including 850-hPa relative vorticity, 200-850-hPa vertical shear of zonal wind, moist static energy, 500-hPa zonal wind, 500-hPa and 850-hPa geopotential height and 200-hPa divergence, are generally less favourable in BB and fewer intense cyclones are observed during OND. The reverse occurs during a La Niña event. However, causes of the variability of TC activity over BB during April-May-June and that over Arabian Sea have yet to be found, which may be due to the small sample size. An example of the correlations between TC activity and various climate parameters is given in Table 1. Details can be found in Ng and Chan (2011).

Table 1. Correlation coefficients between climatic oscillation and TC parameters over the entire North Indian Ocean (NIO) basin (top), Bay of Bengal (BB, middle) and Arabian Sean (AS, bottom) during the period of October-December (OND). Numbers in italic indicate correlations that are statistically significant at the 95% confidence level. Both Niño 3.4 index and Indian Dipole Model index (DMI) are averaged over the period of OND. NTC: number of TCs, ACE: accumulated cyclone energy and NIC: number of intense cyclones (maximum sustained winds ≥ 64 knots).

	NTC	ACE	NIC
NIO			
Niño 3.4	-0.14	*-0.68*	*-0.60*
DMI	*-0.47*	*-0.48*	*-0.48*
BB			
Niño 3.4	-0.23	*-0.66*	*-0.61*
DMI	*-0.41*	-0.36	*-0.48*
AS			
Niño 3.4	0.13	0.05	0.05
DMI	-0.05	-0.19	-0.03

Southern Hemisphere
(PI: Johnny CHAN)

This study examines the interannual variability of the tropical cyclone (TC) activity in the Southern Hemisphere (SH) and develops a seasonal forecast scheme for the number of TCs affecting the Australian region.

This study examines the interannual variability of the tropical cyclone (TC) activity in the Southern Hemisphere (SH) during the period 1970–2008. An empirical orthogonal function analysis of the annual frequency of TC occurrence shows three leading modes of TC occurrence patterns (Figure 3). The first mode, which is related to the El Niño–Southern Oscillation (ENSO) phenomenon, shows an east-west oscillation between the anomalous TC activity over the South Pacific and the South Indian Ocean. The second mode, characterized by an east-west dipole of anomalous TC activity over the South Indian Ocean, is apparently related to both ENSO and the Indian Ocean Dipole (IOD). The third is a basin-wide mode that represents the overall TC activity in the SH.

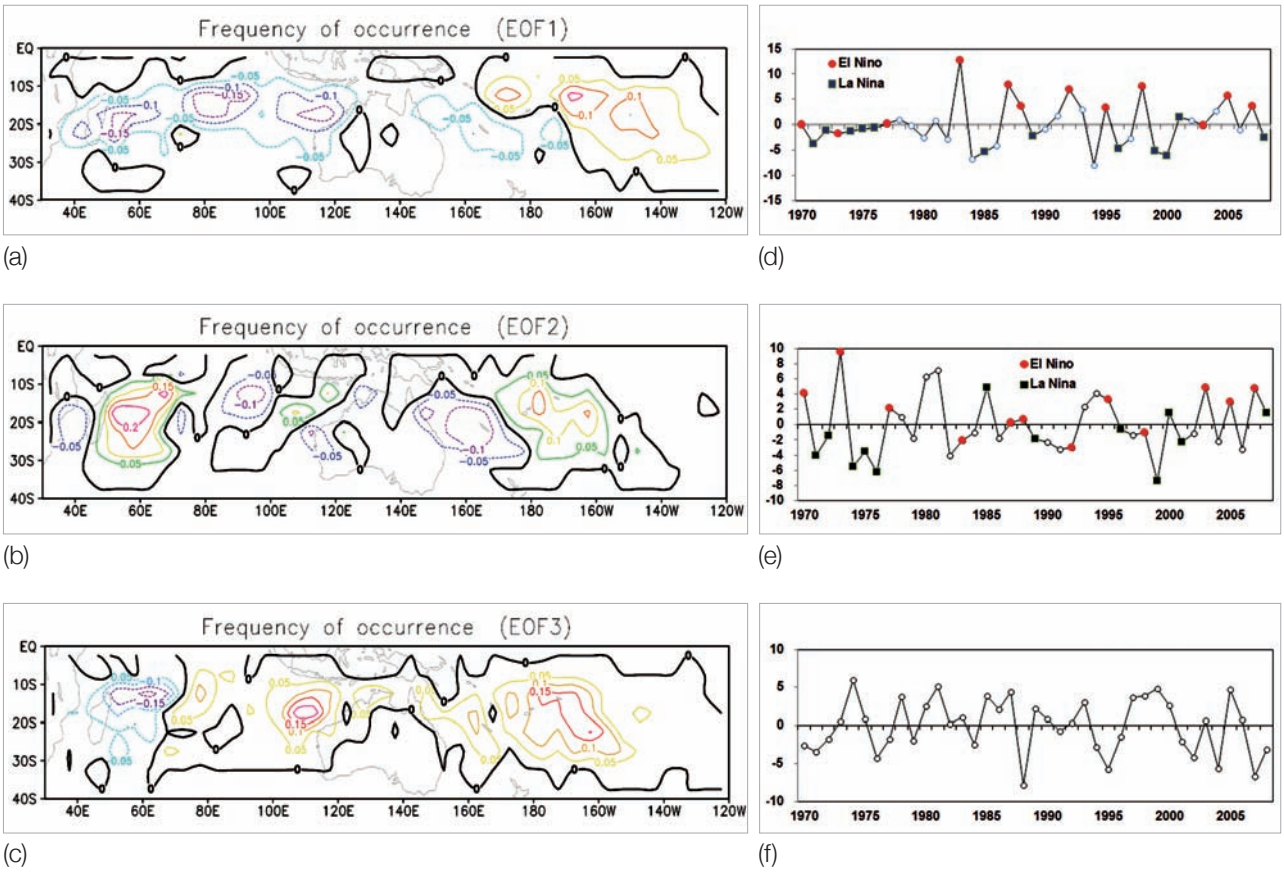

Figure 3. Loading patterns of anomalous TC frequency of occurrence for (a) EOF1, (b) EOF2 and (c) EOF3. Time series of PC1, and PC2 and PC3 are shown in (d)-(f) respectively.

Within the SH, TC activity in the Australian region is found to be related to ENSO and IOD, with the relation being more prominent for the western Australian region. Based on the ENSO- and IOD-related predictors such as Niño-4 SST anomaly, trade wind index, outgoing long wave radiation index and dipole mode index, a statistical prediction scheme for the annual number of TCs in the entire Australian region (40°S–0°N, 90°E–160°E), the western Australian region (40°S–0°N, 90°E–135°E) and the eastern Australian region (40°S–0°N, 135°E–160°E) by 1 November is proposed. This scheme gives a 51%, 39% and 37% skill improvement in root-mean-square error relative to climatology for the three regions respectively. Scatterplots of the predicted versus observed number of TCs are shown in Figure 4. Details can be found in Liu and Chan (2010).

(a) Entire Australian region

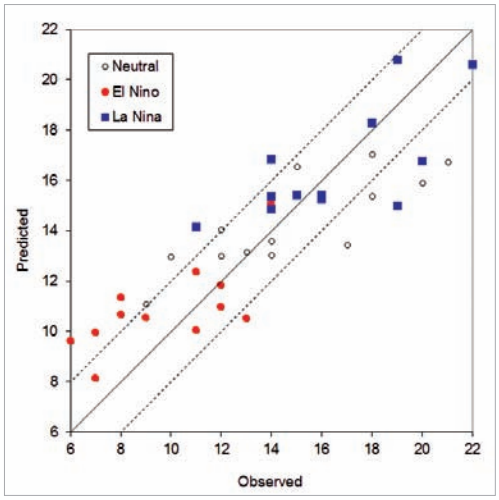

(b) Western Australian region

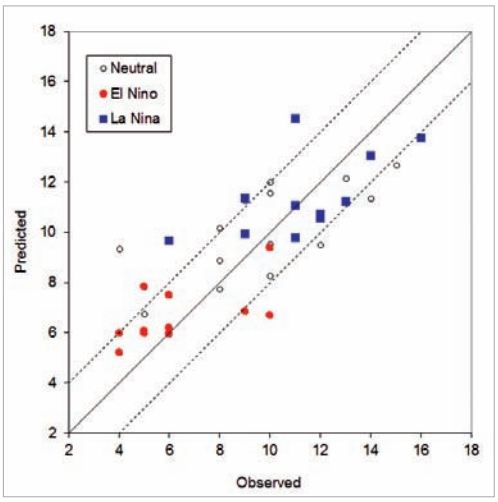

(c) Eastern Australian region

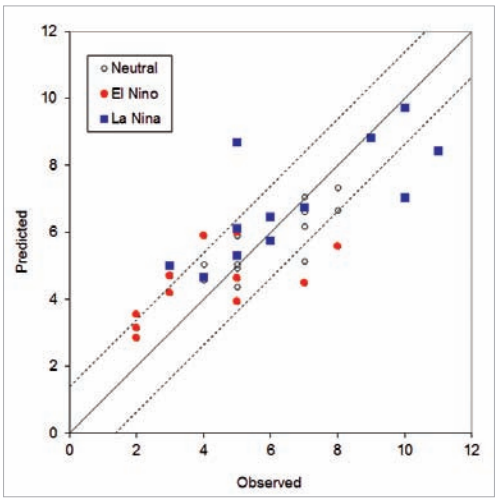

Figure 4. Scatterplot of the hindcasted vs observed values for the number of tropical cyclones in (a) the entire Australian region, (b) the western Australian region and (c) the eastern Australian region. The solid line represents the prefect prediction and the two dashed lines are parallel to the solid line and deviate from it by a value that corresponds to the standard error of the predictions. Solid circles and squares indicate the TC seasons associated with the El Niño and La Niña events.

References:

Goh, A. Z. C. and J. C. L. Chan, 2010: An improved statistical scheme for the prediction of tropical cyclones making landfall in South China. *Wea. Forecasting*, **25**, 587-593.

Goh, A. Z. C. and J. C. L. Chan, 2011: Variations and Prediction of the Annual Number of Tropical Cyclone Affecting Korea and Japan. *Int'l J. Climatology*, DOI: 10.1002/joc.2258.

Liu, K. S. and J. C. L. Chan, 2003: Climatological characteristics and seasonal forecasting of tropical cyclones making landfall along the South China coast. *Mon. Wea. Rev.*, **131**, 1650-1662.

Liu, K. S. and J. C. L. Chan, 2010: Interannual variation of Southern Hemisphere tropical cyclone activity and seasonal forecast of tropical cyclone number in the Australian region. *Int'l J. Climatology*, DOI: 10.1002/joc.2259.

Ng, E. K. W. and J. C. L. Chan, 2011: Interannual variations of tropical cyclone activity over the North Indian Ocean. *Int'l J. Climatol.*, doi: 10.1002/joc.2304.

B. Monsoon studies

1. Monsoon Climate

Winter Monsoon
(PI: Wen ZHOU)

An EOF analysis of the Northern hemisphere circulation shows that the wintertime blocking activity over Siberia is strongly related to the strength of the East Asia winter monsoon.

There are four major modes of atmospheric circulation patterns over the Eurasian Continent (Figure 5). They illustrate the spatial and temporal impacts of blocking activity on the regional climate. When the blocking activity is higher over the Ural-Siberia region, the associated EAWM is stronger (Figure 5b, EOF1 negative). Under the dominance of a blocking system, the strengthened northerly cold advection along its downstream cyclonic component enhances the mass convergence in the upper troposphere leading to intensification of the Siberian high near the surface. The larger horizontal vorticity gradient under the blocking-type circulation tends to push the cold surge southward with a large meridional extent. This common pathway is signified by a sharp northwest-southeast oriented cold anomaly pattern. On the contrary, a weaker EAWM may result from lower blocking activity in the upstream and suppressed convection over the western North Pacific (Figure 5a, EOF1 positive). The reduction of mass convergence from the north and the south near Siberia inhibits the sinking motion and Siberian high development. Consequently, widespread warming probably occurs in East Asia arising from infrequent and weak cold air activity. When the East Asian Trough is stronger, which may be due to higher occurrence frequency of Pacific blocking, the cold surge is likely to take a southeastward pathway bringing a sharp drop of temperature to southern China. This may give rise to a "warm north-cool south" pattern (Figure 5c, EOF2 positive). The fourth mode is a close-to-normal EAWM in an active blocking season over Europe (Figure 5d, EOF2 negative). Despite very high cold air activity in the Middle East and Central Asia, the cold surge frequency in East Asia seems to be normal. This may be regarded as the limited spatial impact of a blocking high on the downstream cold weather in general sense.

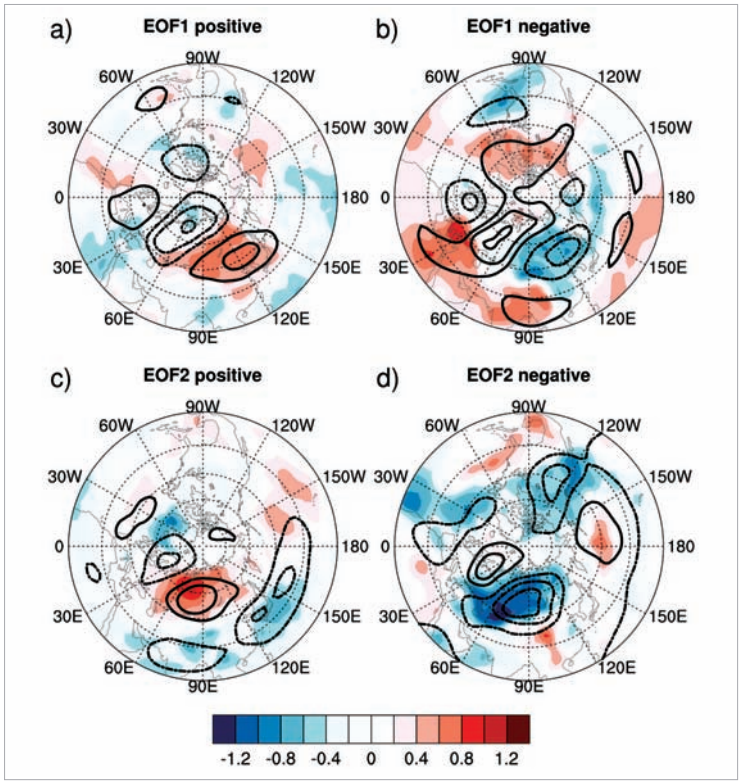

Figure 5. Composite maps for 1000-hPa air temperature anomaly (shading) and 500-hPa geopotential height anomaly (contour) for the years demonstrating dominance in specific polarity of the first two leading EOF modes of the 500-hPa geopotential height over the Eurasian Continent. Contour interval: 0.4 (dimensionless).

Summer Monsoon
(PI: Wen ZHOU)

The strength of the atmospheric water vapor transport over east China is found to be related to the decadal shift in rainfall.

Summer rainfall over East China has experienced two notable transitions over the past few decades. After 1978/79, northward water vapor transport over East China weakened. Anomalous anticyclonic moisture circulation associated with decreasing water vapor divergence is linked to the below-normal precipitation trend over South China (SC) (Figure 6). Strengthened eastward water vapor transport and the anomalous southward transport to the north are associated with an abrupt increase of rainfall over the Yangtze-Haihe River valley (YH). Weakened northward water vapor transport results in a decrease in rainfall over North China (NC). After 1992/93, the convergence of the warmer tropical water vapor from the south with the colder subtropical anomalous water vapor resulted in obvious rainfall variations over SC and the Yangtze River basin. The decadal variations of regional moisture budget also strongly correspond with such a decadal shift of rainfall. Furthermore, it is the meridional water vapor fluxes that play a key role during two rainfall decadal regime shifts over three regions. More detailed information refer to Li et al. (2011).

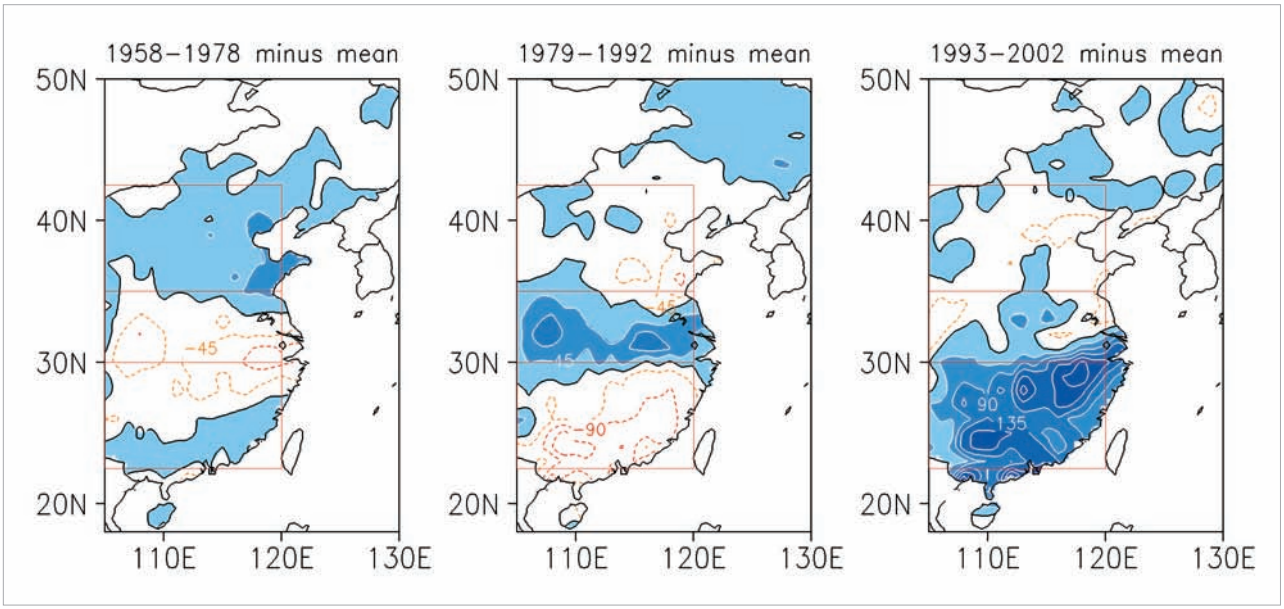

Figure 6. Spatial distribution of summer rainfall (JJA, mm) anomalies over East China during 1958-1978(a), 1979-92(b) and 1993-2002(c) subjected to 1958-2002 mean. The contour interval is 45 mm. Shading denotes value >0 mm. The solid frames represents three regions defined in this study, that is, North China (NC, 35-42.5°N, 105-120°E), Yangtze-Huaihe River valley (YH, 30-35°N, 105-120°E) and Southeast China (SC, 22.5-30°N, 105-120°E).

Reference:

Li, X. Z., Z. P. Wen and W. Zhou, 2011: Long-term Change in Summer Water Vapor Transport over South China in Recent Decades. *Journal of the Meteorological Society of Japan*, **89A**, 271-282, DOI: 10.2151/jmsj.2011-A17.

2. Different Impacts of El Niño and El Niño Modoki on China Rainfall in the Decaying Phases

(PI: Francis TAM)

It is well recognized that ENSO is an important predictor of summer monsoon over China. However, little is known about the difference between the impacts of El Niño and El Niño Modoki on China Rainfall. Here we delineate their influences based on historical station rainfall records in China from 1951 to 2008.

El Niño/Southern Oscillation is one main contributor of tropical climate variability. Recently, a new type of El Niño called El Niño Modoki, has been identified (Ashok et al. 2007; Kao and Yu 2009; Kug et al. 2009). This study examines the impacts of El Niño and El Niño Modoki on the spring and summer rainfall over China, during their decaying phases. During spring in the decaying year of El Niño events, there are positive rainfall anomalies south of the Yangtze River. The wet signal south of the Yangtze River continues in the subsequent summer season, while suppressed rainfall now appears in the more northern Yangtze-Huaihe River region (Figure 7). In contrast, no obvious rainfall signals are found in spring during decaying El Niño Modoki. In the following summer, however, the rainfall is above normal in the region from the Huaihe River to the Yellow River, below normal in southern China.

The distinct China rainfall anomaly is mainly attributed to the difference between the evolution and location of the anomalous western North Pacific (WNP) anticyclone associated with El Niño and El Niño Modoki events. For the case of El Niño, the anomalously strong western north Pacific anticyclone brings more moisture to southern China during decaying El Niño (figure not shown). On the other hand, during the spring of El Niño Modoki events, the anomalous WNP anticyclone becomes weak. In summer, however, the WNP anticyclone intensifies and extends more northwestward towards the in-land region, leading to drier-than-normal conditions in southern China (figure not shown). Further details can be found in Feng et al. (2010).

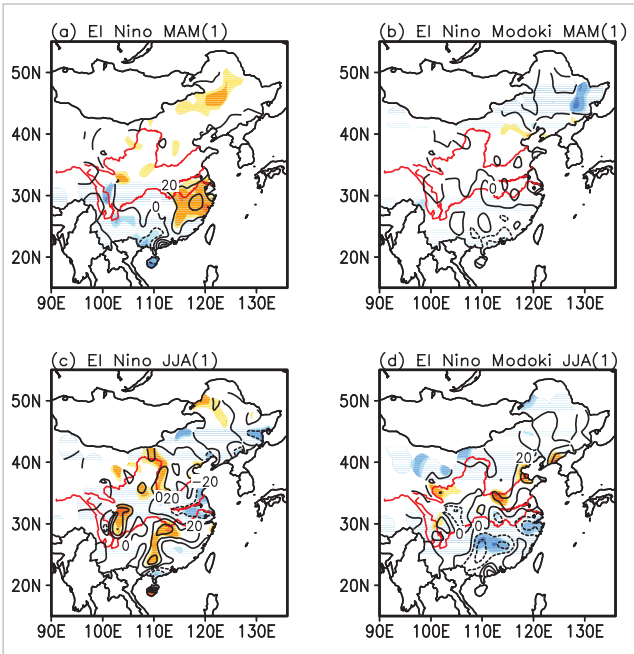

Figure 7. Composite precipitation anomalies during (a, c) MAM (1) and (b, d) JJA (1) in decaying El Niño and El Niño Modoki cases. Contour interval is 20mm. The shading indicates 95% confidence level, respectively.

References:

Ashok, K., S. Behera, S. Rao, H. Weng and T. Yamagata, 2007: El Niño Modoki and its possible teleconnection. *Journal of Geophysical Research*, **112**, C11007, DOI: 10.1029/2006/JC003798.

Feng, J., W. Chen, C.-Y. Tam and W. Zhou, 2010: Different impacts of El Niño and El Niño Modoki on China rainfall in the decaying phases. *Int. J. Climatol.*, DOI: 10.1002/joc.2217.

Kao, H. Y. and J. Y. Yu, 2009: Contrasting eastern-Pacific and central-Pacific types of ENSO. *J. Clim.*, **22**, 615-631. doi:10.1175/2008JCLI2309.1.

Kug, J., F. Jin and S. An, 2009: Two types of El Niño events: cold tongue El Niño and warm pool El Niño. *Journal of Climate*, **22**, 1499–1515.

3. Understanding the Impacts of El Niño and El Niño Modoki on the Western North Pacific Summer Monsoon

(PI: Francis TAM)

The Asian monsoon system is a very important component of the climate system. Understanding its variability associated with ENSO is of great interests of its own, and can lead to better prediction of its behaviour a season or more ahead.

The present study seeks to understand why the western north Pacific monsoon behaves differently during conventional El Niño and El Niño Modoki events. During developing El Niño Modoki in summer, there is enhanced monsoon rainfall covering part of the South China Sea, the Philippines and a broad region in the western north Pacific. In contrast, summertime rainfall at about 150°E, 20°N is suppressed during El Niño. Observations indicate the presence of an anomalous low-level cyclone as early as spring during Modoki events, which might be conducive for a more robust monsoon in mid summer. During El Niño events, the spring-to-early-summer circulation is characterized by anomalous sinking motion and drying over the Philippines and the western north Pacific. To understand how different ENSO-induced heating patterns can lead to different circulation responses, anomaly model experiments were carried out. In boreal spring, the central Pacific heat source generates a low-level cyclone to its west during Modoki events. However, during El Niño it fails to reach the Philippines region due to the divergent and anti-cyclonic flow associated with the heat sink there (Figure 8). These simulations results are in accordance with observations, and they account for the different dynamical interactions between the monsoon and the two types of ENSO in the subsequent summer season.

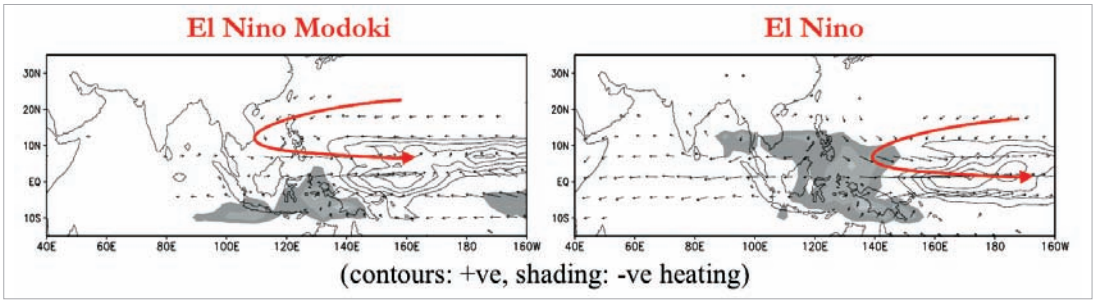

Figure 8. Anomaly model wind response at 850 hPa (arrows; see scale arrow at bottom; units: ms^{-1}) to prescribed heating anomalies (contours and shading for positive and negative values, respectively, at the level of maximum heating; interval: 0.2°C/day; zero contours are omitted) for El Niño Modoki (left) and El Niño (right) during the April-to-June period.

C. Monsoon-Typhoon Interaction

1. Asymmetric Modulation of the Western North Pacific Cyclogenesis by the Madden-Julian Oscillation under ENSO Conditions

(PI: Wen ZHOU)

The intensified MJO-TC relationship in El Niño years is induced by the synchronization and reinforcement of the ENSO-related and the MJO-induced favorable conditions during the active phase.

This study investigates the modulation by the Madden-Julian Oscillation (MJO) and the impact of El Niño-Southern Oscillation (ENSO) on the tropical cyclone (TC) genesis in the Western North Pacific (WNP) during the period from 1979 to 2006 (Figures 9-10). Significantly more (fewer) TCs are found in the active (inactive) MJO phase in the southern part of WNP (south of 15°N). It is proposed that the strong MJO westerlies (easterlies) in the active (inactive) phase, which plays a more important role than convection and vorticity, induce an enhanced (weakened) monsoon trough that leads to significant enhancement (suppression) of TC formation in the southern part of WNP.

Another key finding in this study is that the MJO modulation on cyclogensis is strengthened during the El Niño conditions especially in the southeast quadrant (0°-15°N, 140°-180°E). During the La Niña years, however, no significant modulation is found, indicating a weakened MJO-TC relationship. We propose that the intensified MJO-TC relationship in El Niño years is induced by the synchronization and reinforcement of the ENSO-related and the MJO-induced favorable conditions during the active phase as well as the domination of the unfavorable MJO conditions during the inactive phase. In contrast, the La Niña events provide dominant unfavorable background conditions, the easterlies anomalies, in the southern part of WNP. And the impact of MJO is weaker and cannot reach the northern part of WNP with major TC formations during La Niña years. These lead to the overall weakened MJO-TC relationship. It is expected that this study will have some implications on improving the seasonal forecast of TCs in the WNP. More detailed information refer to Li et al. (2011).

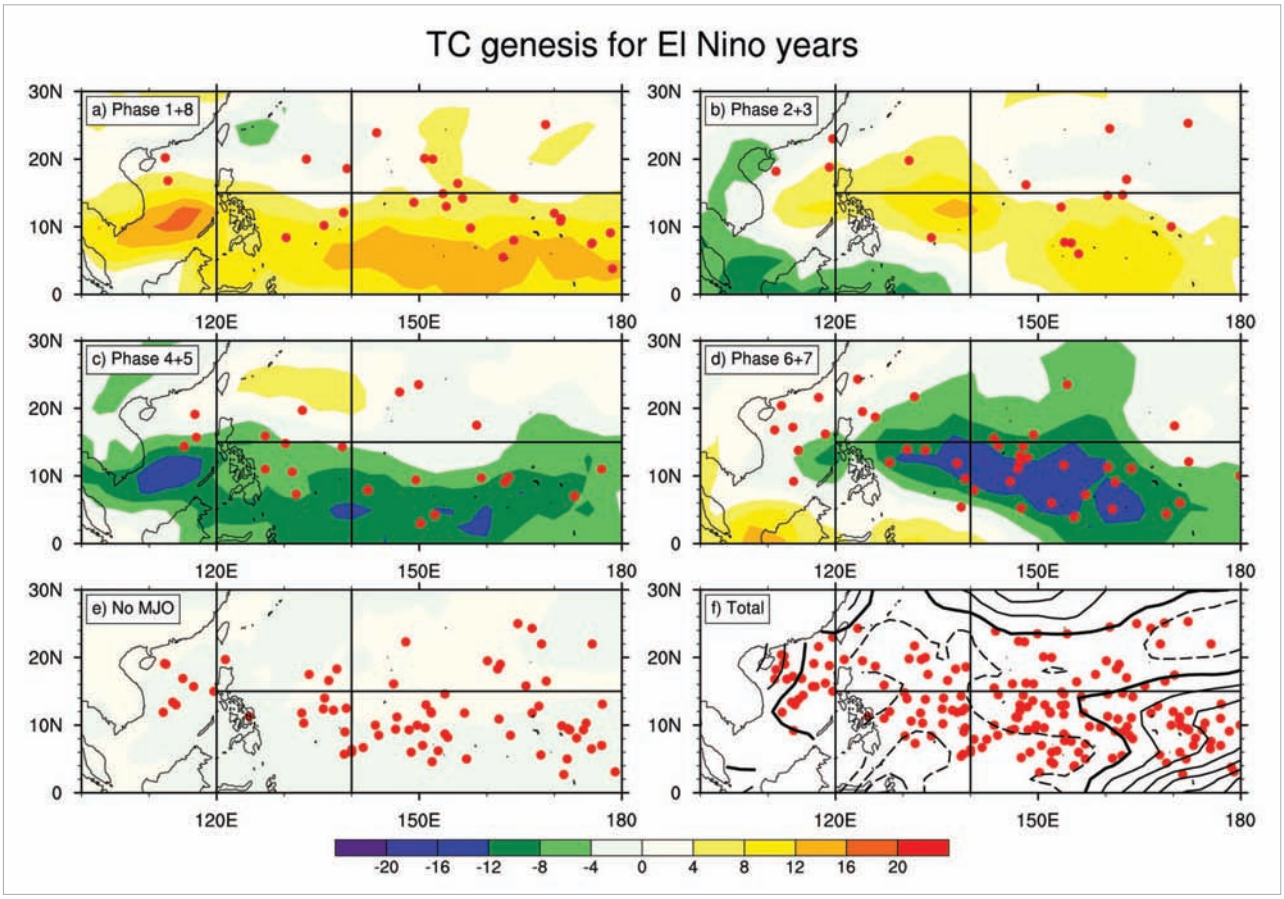

Figure 9. Composites of 20-90 day filtered OLR anomalies (shading; units: W/m^2) and SSTA (dash/solid contours indicating negative/positive values and the solid thick line denoting zero contour; contour interval 0.08°C) with the distribution of tropical cyclones (denoted by red circles) for different MJO phase categories (a) category "1+8", (b) category "2+3", (c) category "4+5", (d) category "6+7", (e) No MJO, (f) Total for the 7 El Niño years in the TC season during 1979-2006.

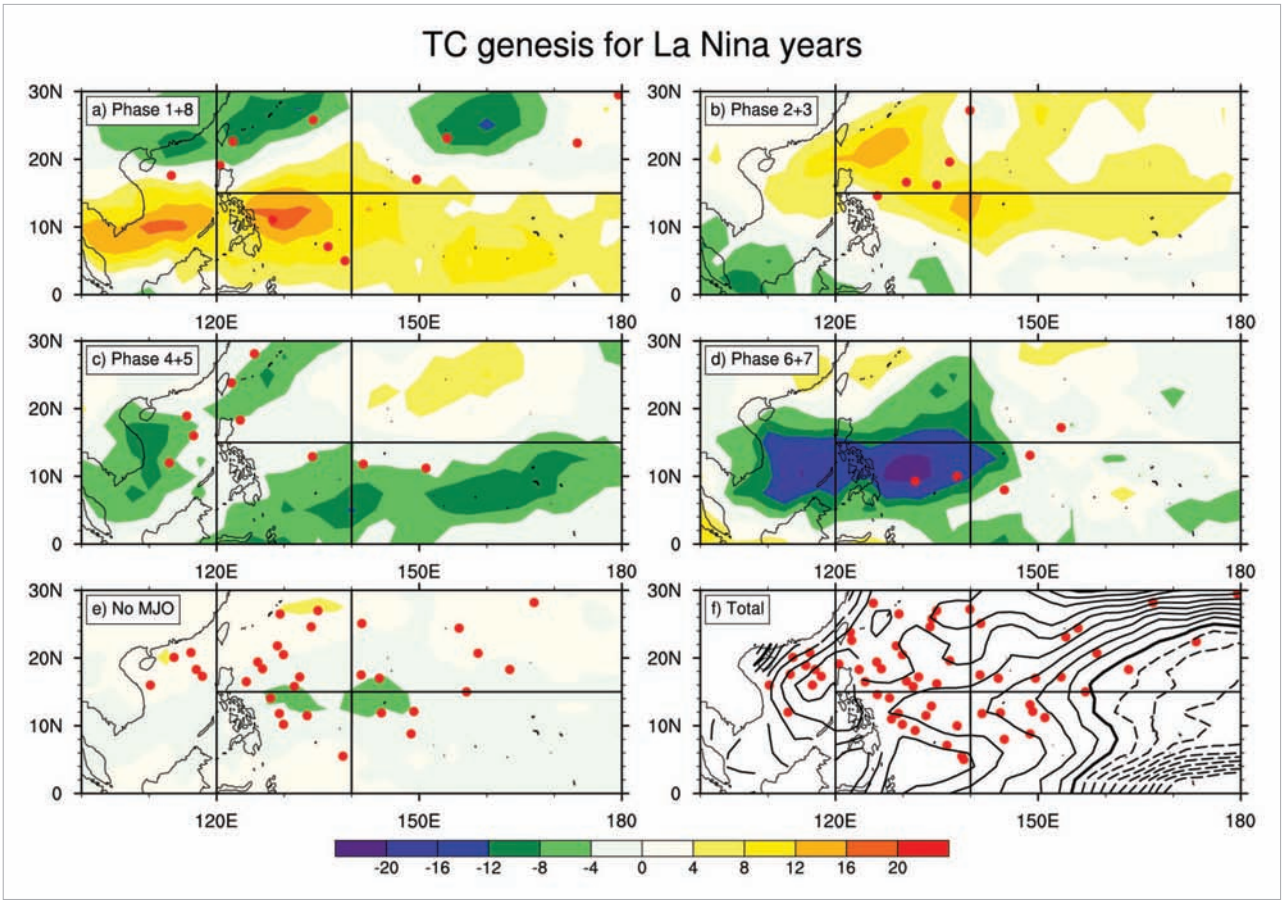

Figure 10. Composites of 20-90 day filtered OLR anomalies (shading; units: W/m2) and SSTA (dash/solid contours indicating negative/positive values and the solid thick line denoting zero contour; contour interval 0.08°C) with the distribution of tropical cyclones (denoted by red circles) for different MJO phase categories (a) category "1+8", (b) category "2+3", (c) category "4+5", (d) category "6+7", (e) No MJO, (f) Total for the 3 La Niña years in the TC season during 1979-2006.

Reference:

Li, C. Y., W. Zhou, J. C. L. Chan and P. Huang, 2011: Asymmetric modulation of the Western North Pacific cyclogenesis by the Madden-Julian Oscillation under ENSO conditions. *International Journal of Climatology*. (Under revision)

2. Seasonality of Super Typhoon Activities in the Western North Pacific

(PI: Wen ZHOU)

This study investigates the seasonality of Super Typhoon (STY) (Cat4 and Cat5) activities in the Western North Pacific (WNP) in the period of 1979-2006 using JTWC (Joint Typhoon Warning Center) datasets. The results suggest that tropical cyclones formed in the late season especially in November have a higher chance to develop into STYs and the STYs formed can attain higher intensity compared to their summer counterparts. This can be attributed to the higher positive vorticity and lower vertical shear in the late season which are more favourable for STY development (Figure 11).

Tropical cyclones formed in the late typhoon season have a higher chance to develop into super typhoons.

Besides, the interannual variability of the STY activities is also investigated. The ENSO impact on the STY number is found to be stronger during the early season (Jul-Aug) compared to the late season (Sep-Nov). This is mainly due to the significant reduction in STY number in the early season of the La Niña years which can be attributed to the variation in the position and strength of the monsoon trough. It is hoped that this study can contribute some new insights into the seasonal and interannual variations of STYs in the WNP.

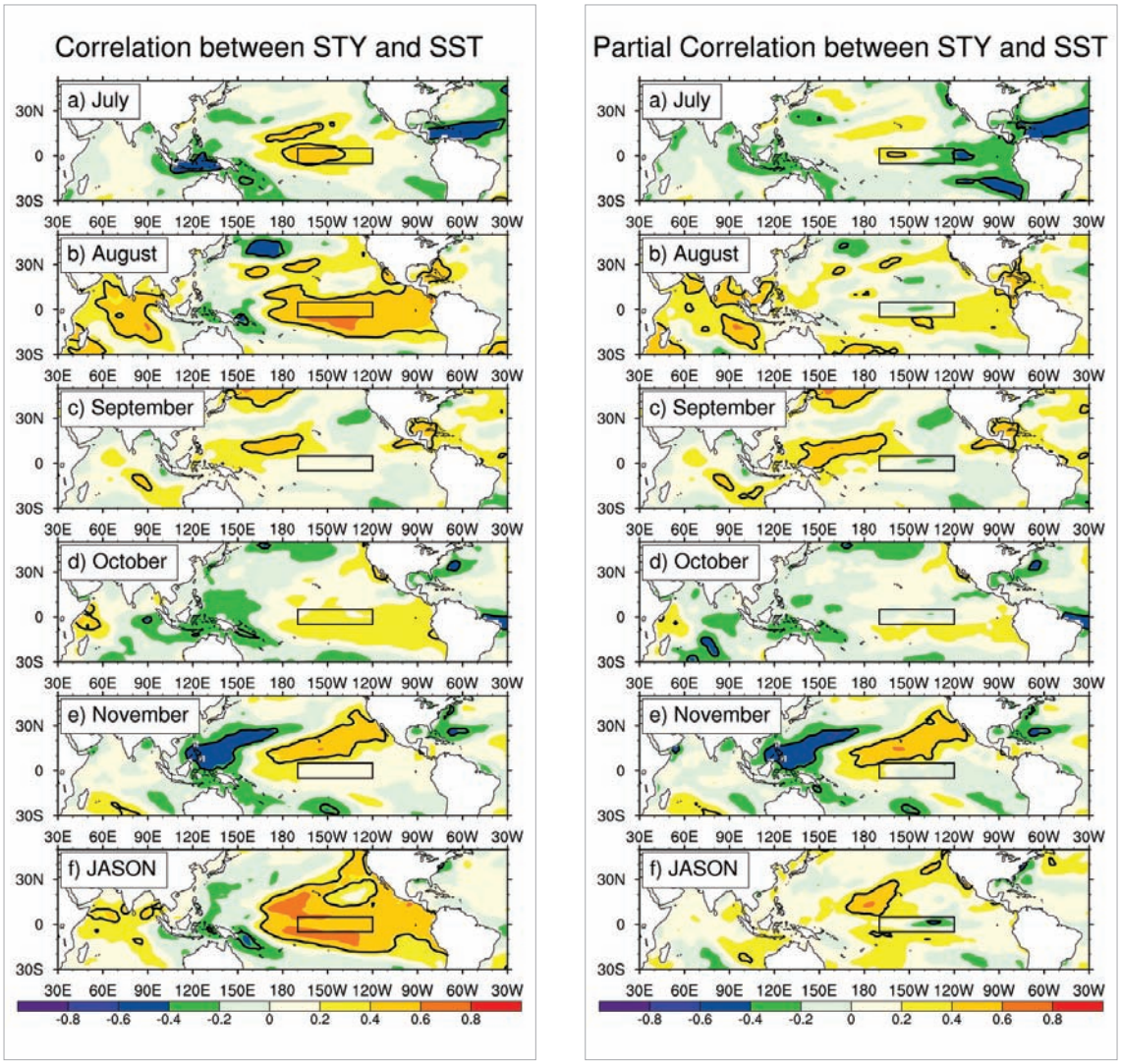

Figure 11. Simultaneous correlation and partial correlation (after removal of ENSO impact) between the STY number and the sea surface temperature. The box denotes the Niño3.4 region while the thick solid line denotes 90% confidence.

3. High-Resolution Model Simulations of the Impact of ENSO Modoki on the Western North Pacific Monsoon and TC Activity

(PI: Francis TAM)

The ability of high-resolution general circulation models in capturing both changes in the larges-scale monsoon circulation and TC activity is examined in this study. These models can be a useful tool in understanding and predicting the future climate and extreme events behaviour in the Asian region.

In this on-going project, we have carried out atmospheric GCM experiments using ECHAM5 with T159 horizontal resolution (about 75 x 75km), in order to study how El Niño Modoki affects the western north Pacific summer monsoon and TC activity in a model environment. In particular, AGCM simulations with prescribed Modoki-like

SST anomalies have been compared with control runs using climatological SST values. It is found the model can broadly reproduce ENSO Modoki's influence on the summer monsoon circulation over the East Asian/western north Pacific region. Typical Modoki impacts such as increased monsoon rainfall from the Bay of Bengal to the western north Pacific, and the accompanying enhanced low-level westerly flow, were found in the model runs. There was also an increase in the basin-mean model TC genesis frequency during Modoki events, compared with climatology. This result is also consistent with observations. We are now carrying our further analysis in order to understand the dynamical reasons behind the change of TC genesis in the model simulations.

D. Diurnal Variations

1. Semi-Diurnal Variations in Rainfall over Southeast China

(PI: Johnny CHAN)

This study investigates the mechanism for the early morning maximum in rainfall over Southeast China in the summer. Late-night vertical differential thermal advection and the semi-diurnal variation of land-sea differential radiative heating/ cooling are found to be the major reasons for the enhancement of such a phenomenon.

During the summer months, diurnal rainfall variation over the Southeast China is frequently characterized by a major peak in the afternoon and a minor peak in the early morning (Figure 12). While the afternoon rainfall maximum is generally recognized to be mainly modulated by the diurnally-varying wind introduced by the land-sea and mountain-valley differential heating, causes of the early morning rainfall remain not well documented. In this study, the variation of semi-diurnal harmonic of rainfall is found to be more important than the variation of diurnal harmonic of rainfall for determining the timing of early morning rainfall peak. Diagnoses of the atmospheric thermodynamic conditions indicate that the late night vertical differential thermal advection and the semi-diurnal variation of land-sea differential radiative heating/cooling are the major reasons for reducing the stability in the early morning and, in turn, facilitates the formation of an early morning maximum in rainfall (Figure 13). Computation of the water vapor budget suggests further that the early morning maximum over Southeast China is mainly maintained by the semi-diurnal harmonic of water vapor flux transporting from the South China Sea.

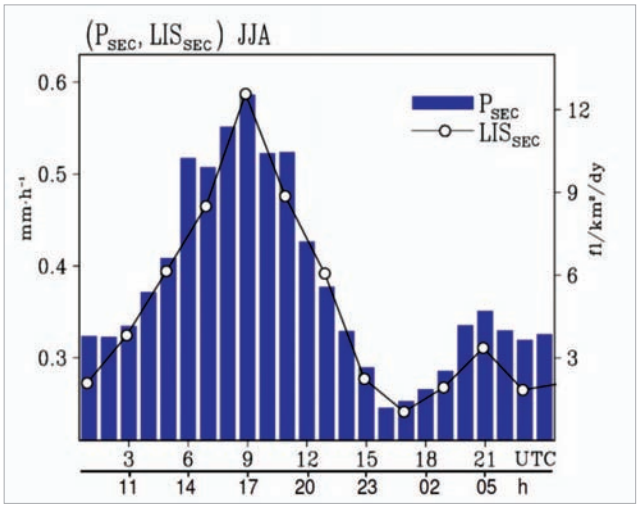

Figure 12. Temporal variations of JJA-mean hourly precipitation (*P*; histogram; scale on the left ordinate) and 2-hourly lightning activities (LIS; solid line with open circles; scale on the right ordinate) area-averaged over Southeast China [SEC; 110°E-118°E, 21°N-25°N]. Local time in SEC is universal time (UTC) + 8 h.

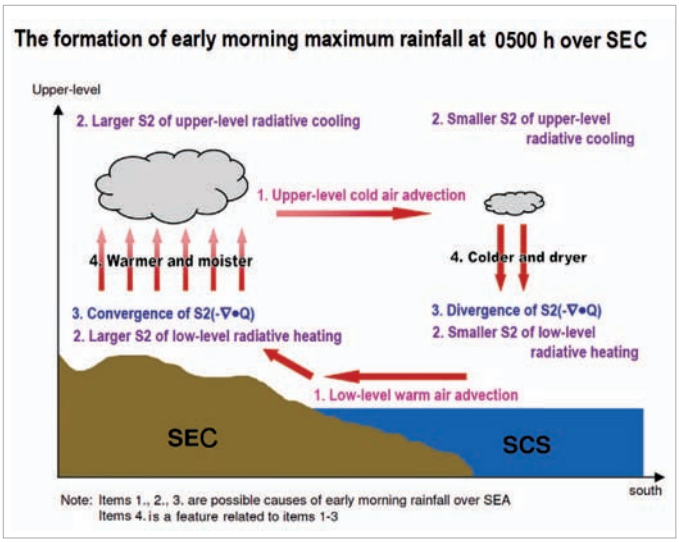

Figure 13. A schematic diagram illustrating the formation of early morning maximum rainfall over SEC that induced by the late night vertical differential thermal advection (Item 1), the S2 harmonic of land-sea differential radiation heating/cooling between SEC and SCS (Item 2), and the S2 harmonic of land-sea differential water vapor flux convergence/divergence between SEC and SCS (Item 3). Modulated by these three mechanisms, the atmospheric temperature above SEC at 0500 h is relative unstable than other hours without solar heating (Item 4).

2. Seasonal Variation of Diurnal and Semi-Diurnal Variations in Rainfall over Southeast China

(PI: Johnny CHAN)

Diurnal and semi-diurnal variations in rainfall over Southeast China are found to be caused by different mechanisms in summer and winter.

Diurnal (S1) and semidiurnal (S2) oscillations are major factors in determining the sub-daily variations of precipitation amount over Southeast China (P_{SEC}). Most studies have examined the causes of S1(P)$_{SEC}$ and S2(P)$_{SEC}$ in the summer rainy season. However, causes of the seasonal changes in S1(P)$_{SEC}$ and S2(P)$_{SEC}$ (Figure 14) have not been well documented. This study therefore examines possible mechanisms behind various precipitation types/cloud types because different types of precipitation/clouds control PSEC in different seasons (Figure 15). Results indicate that the variation of S1(P)$_{SEC}$ in winter, which tends to peak in the early morning, is mainly controlled by the high-relative-humidity-induced diurnal variation of non-showery precipitation/middle-level clouds. For S1(P)$_{SEC}$ in the other seasons, which tends to peak at the late afternoon, the moist-convection-induced diurnal variation of showery precipitation/low-level clouds is the main cause. Analyses also suggest that the phase of S2(P)$_{SEC}$ does not vary seasonally because both of its formation mechanisms — the semidiurnal variation of relative humidity and moist convection process — have similar phase evolution in all seasons. Seasonal changes in the water vapor supply to the maintenance of S1(P)$_{SEC}$ and S2(P)$_{SEC}$ are also discussed.

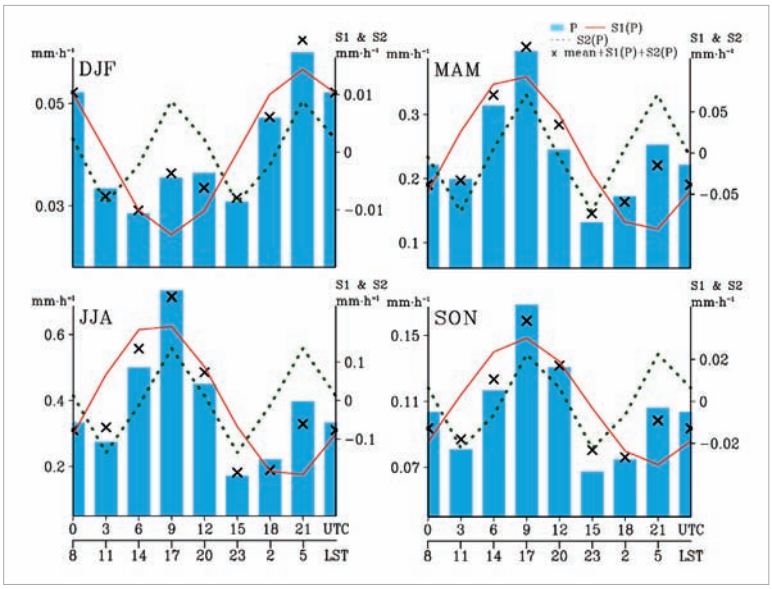

Figure 14. Time evolution of mean 3-hourly P_{SEC} (histogram), diurnal harmonic of P_{SEC} [i.e. S1(P)$_{SEC}$; solid line], semidiurnal harmonic of P_{SEC} [i.e. S2(P)$_{SEC}$; dotted line], and a combination of daily mean, S1 and S2 harmonic of P_{SEC} (denoted by ×) in different seasons of the year. The scale of S1(P)$_{SEC}$ and S2(P)$_{SEC}$ is given on the right, whereas the scale of the other two variables is given on the left. The lower x-axis is local time over SEC, which is universal time (UTC) +8 h.

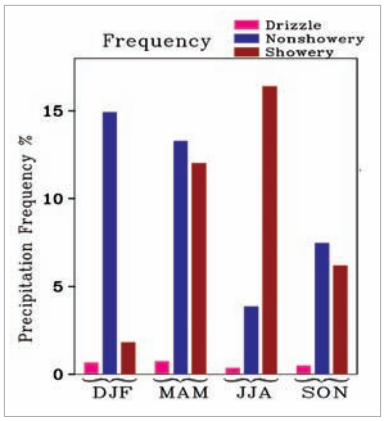

Figure 15. Seasonal mean frequency of occurrence for drizzle, non-showery and showery type of precipitation area-averaged over SEC.

E. Climate Studies

1. A Planetary-Scale Land-Sea Breeze

(PI: Johnny CHAN)

The diurnal wind variation over the East Asian continent is commonly considered to be a combination of a land-sea breeze near the coast and a mountain–valley breeze along the slopes of the Tibetan Plateau with a spatial scale of <100 km. However, a detailed examination of the global reanalysis data suggests that this local land–sea breeze circulation apparently couples with the global-scale diurnal atmospheric pressure tide to produce a planetary-scale land–sea breeze with a spatial scale of ~1000 km over the western North Pacific.

The diurnal wind variation over the East Asian continent is commonly considered to be a combination of a land-sea breeze near the coast and a mountain–valley breeze along the slopes of the Tibetan Plateau. The local land–sea breeze along the coastline typically spans <100 km into the ocean. However, a detailed examination of the global reanalysis data suggests that this local land–sea breeze circulation apparently couples with the global-scale diurnal atmospheric pressure tide to produce a planetary-scale land–sea breeze with a spatial scale of ~1000 km over the western North Pacific. Computations of the momentum budget and equivalent potential temperatures indicate that the atmospheric diurnal tidal wave contributes the most to this circulation feature. A diagnosis of the water vapour budget further suggests that the convergence of water vapour flux, which is related to the convergence of low-level wind induced by the seasonal change of diurnal tidal wave, leads to different times of occurrence of maximum diurnal rainfall over East Asia between summer and winter. An example of this planetary-scale circulation is shown in Figure 16. Details can be found in Huang et al. (2010a).

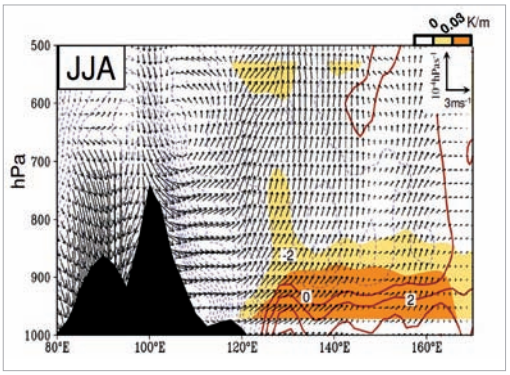

Figure 16. Vertical cross-section of diurnal harmonic of equivalent potential temperature (contoured), $(-(\partial\theta e/\partial z)$; shaded), and $((u, -\omega)$; vector) at 23°–25°N, 0000 UTC for the 1989–2009 summer periods. The contour interval of θe is 5×10^{-2} K.

Reference:

Huang, W.-R., J. C. L. Chan and S. Y. Wang, 2010a: A planetary-scale land–sea breeze circulation in East Asia and the western North Pacific. *Quarterly Journal of the Royal Meteorological Society*, **136**, 1543-1553.

2. Discrepancy among Different Reanalyses

(PI: Johnny CHAN)

This study finds that the discrepancies between the reanalysis datasets and observations can contribute to inconsistent interdecadal variations of the cold surge frequency in different reanalysis datasets.

This study examines the interdecadal variations of the Siberian High (SH) and cold surges deduced from six modern global reanalysis datasets (Figure 17). Previous studies revealed a pronounced decline in the strength of the SH during the late 20th century accompanied with a coherent decrease in the frequency of cold surges. Analyzing six modern reanalyses and observations, this study reports apparent discrepancies in such interdecadal variations. The rapid decline of the SH is found to be considerably less pronounced in all six reanalyses. The associated decrease in the cold surge frequency recorded from stations is also consistently weaker in reanalyses. On the other hand, the interannual variations of both the SH and cold surges are fairly consistent between reanalyses and observations, suggesting that changes in the assimilation process of individual reanalyses may be a factor. In addition, changes in the observing system are also possible to cause the different trends of SH and cold surge frequency between reanalyses. The documented inconsistency of reanalyses in the depiction of the SH and cold surges can cause misinterpretation of the East Asian winter monsoon variability when using these reanalyses and, therefore, deserves attention. Details can be found in Huang et al. (2010b).

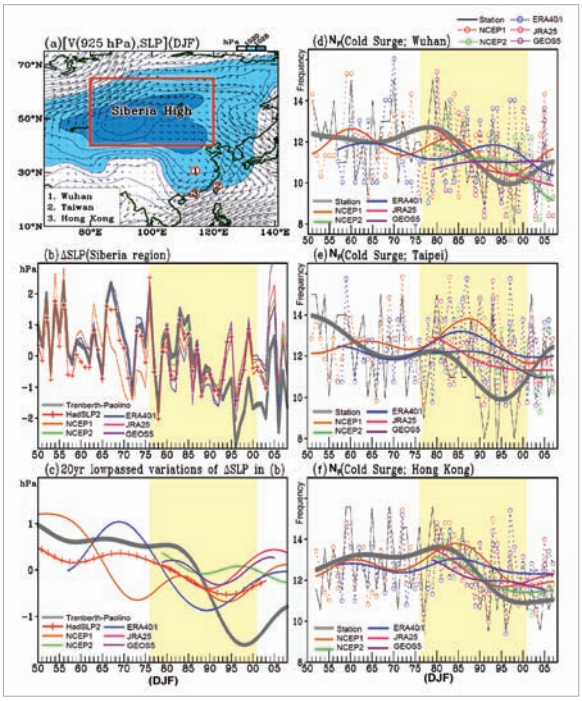

Figure 17. (a). The 925-hPa wind vector superimposed with sea level pressure (SLP) for winter (December to February) climatology averaged over the 1979-2008 period derived from the ERA40/I reanalyses. (b) Time series of the SLP anomalies (ΔSLP) averaged over the Siberia high [(80°E-120°E, 40°N-65°N) as outlined in (a)] from 1950 to 2008 using the observed ΔSLP (Trenberth-Paolino data and HadSLP2) and assimilated ΔSLP (NCEP1, NCEP2, ERA40/I, JRA25, and GEOS5). (c) The 20-yr lowpassed variations of (b). (d)-(f) The wintertime cold surge frequencies (N_F) in Wuhan, Taiwan, and Hong Kong observed from stations and the reanalyses. Solid thin lines (dotted thin lines with open circles) show the actual time series of observed (assimilated) N_F and solid thick lines are the associated 20-yr lowpassed variations. The time period between 1976 and 2001 where the great SH decline was noted is shaded in light yellow.

Reference:

Huang, W.-R., S.-Y. Wang and J. C. L. Chan, 2010b: Discrepancies between global reanalyses and observations in the interdecadal variations of Southeast Asian cold surge. *International Journal of Climatology*, DOI: 10.1002/joc.2234.

3. Climate Extreme Study

Drought
(PI: Wen ZHOU)

11 climatological drought regions within China are classified by using the cluster analysis.

The Standard Precipitation Index (SPI) is a way of measuring drought. It can quantify the precipitation deficit and to reflect the impact of drought on the availability of the different water resources. The calculation procedure is applied to monthly precipitation over different regions of China. A drought event is regarded as a period in which the SPI is negative and the SPI reaches a value of -1.0 or less. The drought begins when the SPI first falls below zero and ends with the positive value of SPI following a value of -1.0 or less. Drought intensity is arbitrarily defined for values of the SPI with the following categories:

SPI Values	Drought Category
SPI<-1.0	mild drought
-1.0≤ SPI<-1.5	moderate drought
-1.5≤ SPI<-2.0	severe drought
SPI≤-2.0	extreme drought

Then the return periods can be estimated by relating the probability distribution for annual maximum series (the largest drought event each year) to the frequency of events in the partial duration series of drought events. Hence, return period curves of a drought of specific severity (deficit) and the corresponding area coverage can be constructed. Furthermore, 11 climatological drought regions within China are classified by using the Cluster analysis (Figure 18). The variations of 11 drought regions are examined. The severe drought that took place in southwest China during Oct 2009 to Apr 2010 is obviously detected in this study (not shown). Note that rainfall in most parts of north and central China was 50 to 80 percent less than normal. The drought is one of the worst in 50 years for these regions. The land is parched and the irrigation dams have dried up. Crops and livestock are dying. The drought has hit 12 provinces, including the wheat-producing areas in Shandong, Henan, Anhui, Guizhou, and Yunnan provinces (Figure 19).

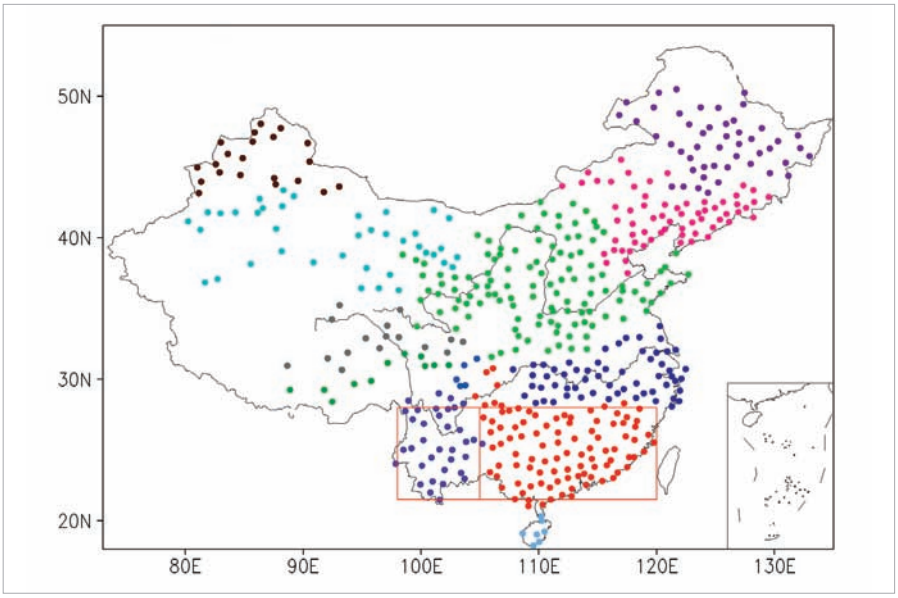

Figure 18. Climatic regions derived from monthly SPI records during 1961-2010 over China by the method of cluster analysis. Solid circles filled with different colors indicate drought regions.

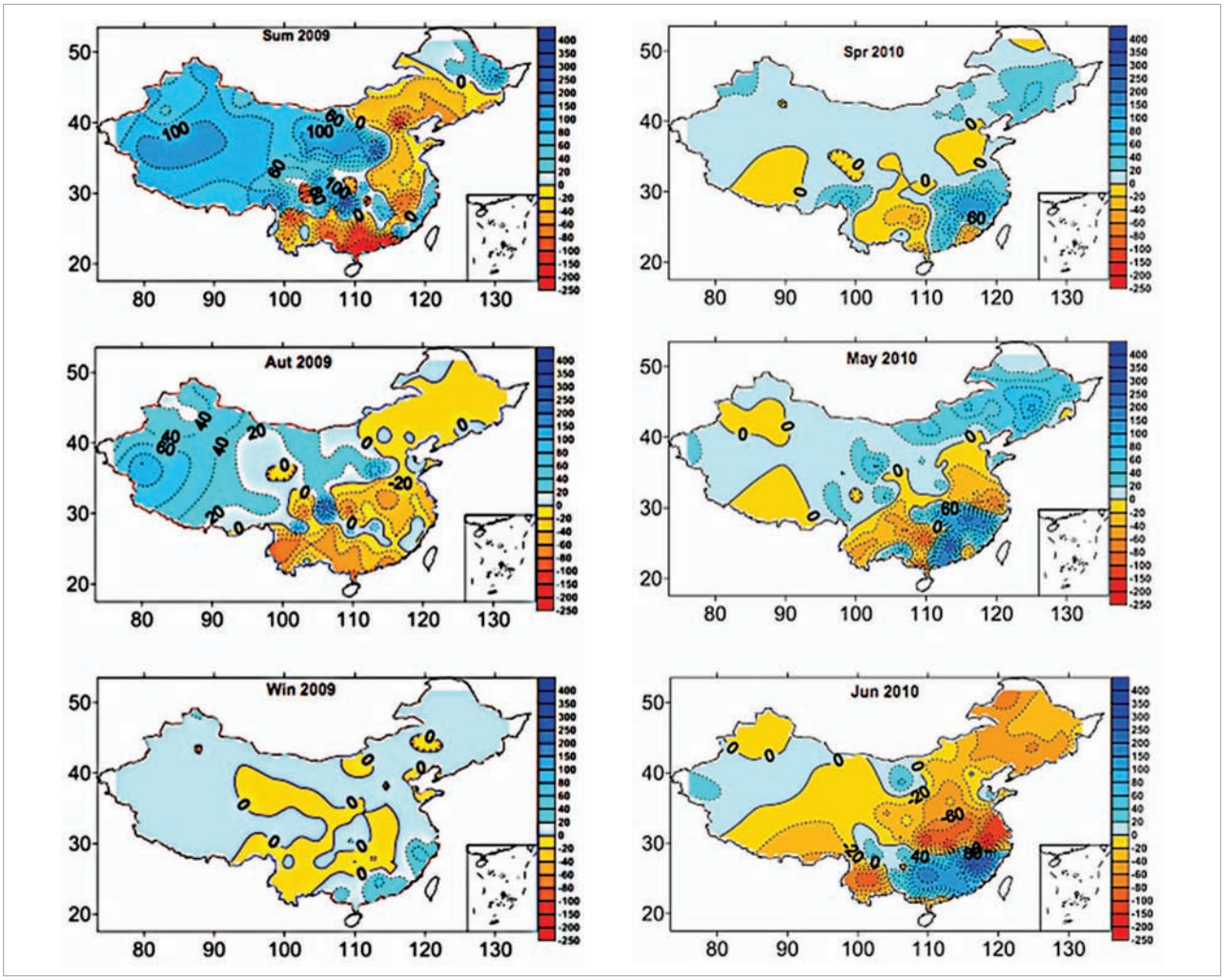

Figure 19. 2009-2010 rainfall anomaly in China with respect to 1971-2000.

Heat Wave
(PI: Wen ZHOU)

High frequency of heat waves in South China is associated with an anomalous strong subtropical high pressure system

The relative definitions in association with a large percentile of the weather observations are adopted in this study based on daily maximum temperature (DMT) records from 1961-2010 over southeast China. This relative definition uses seasonally varying thresholds rather than arbitrary fixed temperature thresholds to define the extreme temperature by transforming each day's temperature to a percentile (return period). The spatial distribution and temporal variation of relative heat wave events over South China are investigated (Figure 20). Summer heat waves of China along the southeast coastline region are significantly related to the subtropical high over the western Pacific (Figure 21). High frequency of heat waves in this area is associated with anomalous strong subtropical high. However, no significant correlation between subtropical high and HWs in other regions of China is found.

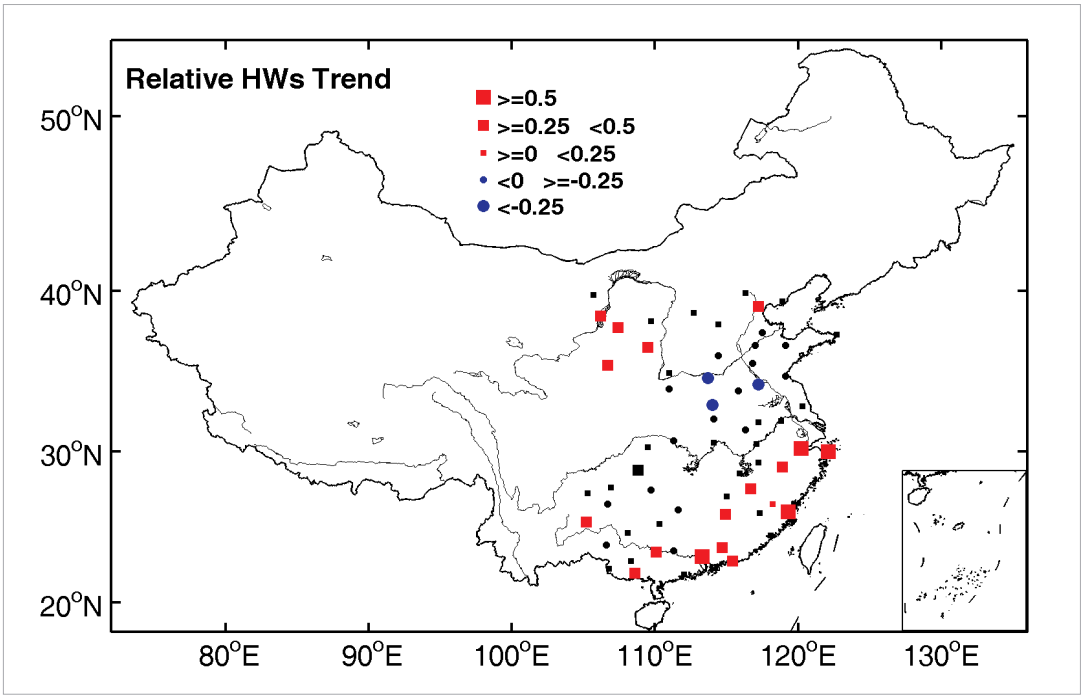

Figure 20. Long term trend of relative heat waves over southeast China. Colored points indicate stations with calculations statistically significant at the 5% level.

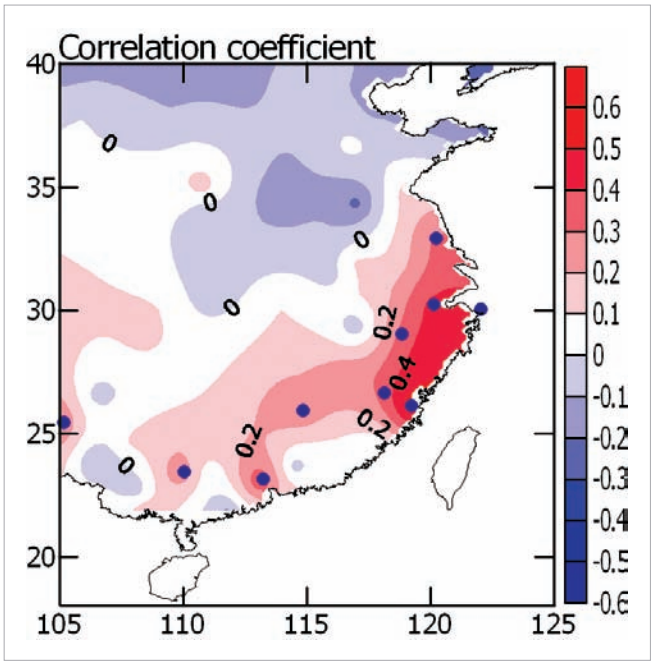

Figure 21. Simultaneous correlation coefficients between relative HWs and the strength of the subtropical high over the western Pacific (110-180°E). Blue points indicate stations with correlations statistically significant at the 5% level.

Local Climate Change and Global Warming (PI: Wen ZHOU)

The summer tends to be longer and winter tends to be shorter in a warming scenario

Changes in seasonality in China under enhanced atmospheric CO_2 concentration were investigated by examing simulations from the 1% per year CO_2 increase experiments of nine global climate models. Simulations of the 20th century experiments of the same models are also assessed, with regard to observed changes in seasonality in China from the period 1961-1980 to 1981-2000. The results show that the ensemble mean simulation of the nine

models performs better than individual model simulations (Figure 22a, b). While the CO_2 concentration increases from doubling to quadrupling of the pre-industrial or present-day level, the ensemble mean results show that the hottest/coldest continuous-90-day (local summer/winter) mean temperature increases by 3.4/4.5°C, 2.7/2.9°C, 2.9/4.1°C in NE, SW, and SE China, respectively, indicating a weakening seasonal amplitude (SA); but by 4.4/4.0°C in NW China, indicating an enhancing SA. The local summer is lengthened by 37/30/66/54 days in NW, NE, SW and SE China, respectively. In some models, the winter disappears according to the threshold based on observations in the late 20th century. The average of other models' simulations shows local winter shortened by 42/36/ 61/44 days in the four regions, respectively. More detailed information refer to Xia et al. (2011).

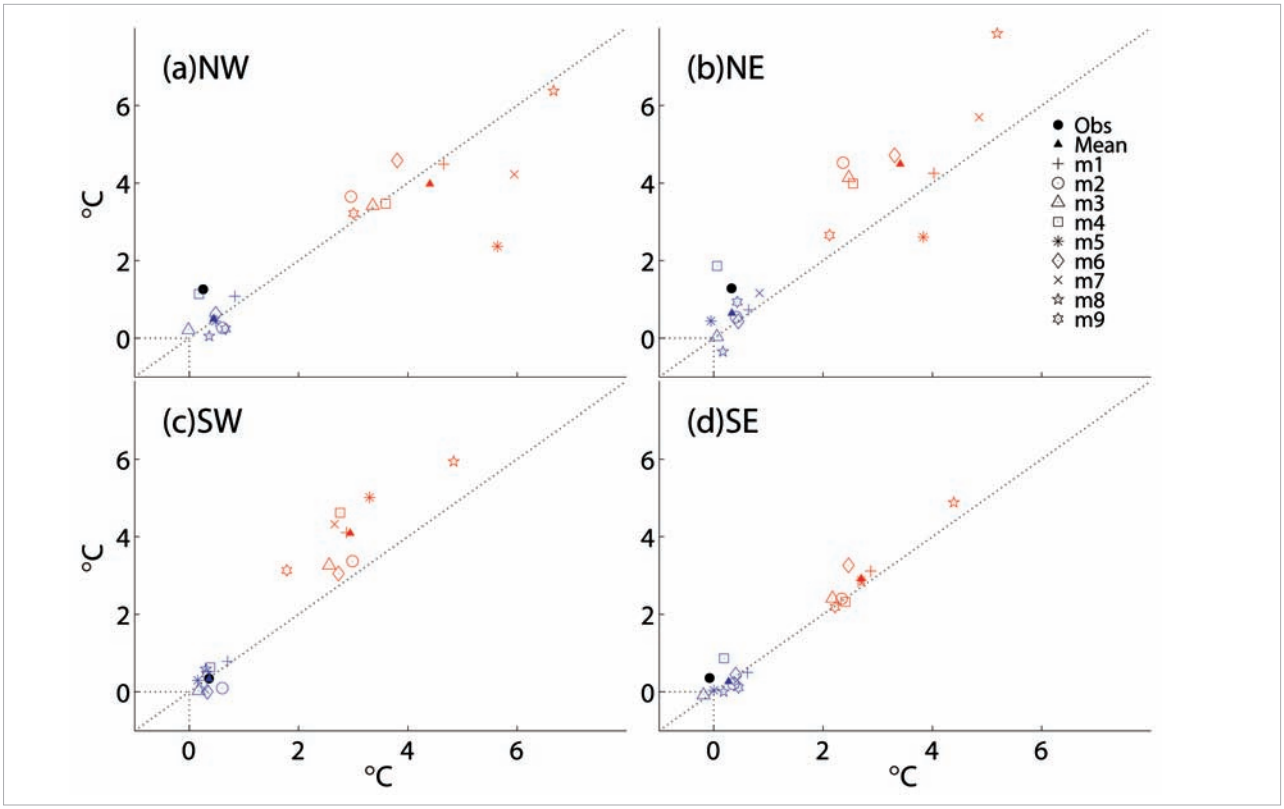

Figure 22a. The temperature increments of ESH (x-coordinate) and ESC (y-coordinate) from Period I to Period II. Black points indicate the experimentally observed temperature. The blue points indicate the simulated results of the 20c3m experiments using nine models; red ones are the results between quadrupling- and doubling-CO_2 experiments. The solid-triangles indicate the mean of results obtained using the nine models. The third generation coupled global climate model (3.1,T47) of Canadian Centre for Climate Modelling & Analysis (CCCMA-CGCM3.1 (T47)), coupled model (3.0) of Centre National de Recherches Meteorologiques, Meteo France, France (CNRM-CM3), coupled model (2.0, 2.1) of Geophysical Fluid Dynamics Laboratory, NOAA (GFDL-CM2.0, GFDL-CM2.1), ModelE-Russell of Goddard Institute for Space Studies, NASA, USA (GISS-MODEL-ER), ECHAM4 model of Istituto Nazionale di Geofisica e Vulcanologia, Italy (INGV-ECHAM4), ECHAM4 + HOPE-G model of Meteorological Institute of the University of Bonn, Germany (MIUB-ECHO-G), ECHAM5 model of Max Planck Institute for Meteorology, Germany (MPI-ECHAM5), coupled global climate model (2.3.2a) of Meteorological Research Institute, Japan (MRI-CGCM2.3.2a), referred to thereafter as m1, m2, …, m9, respectively.

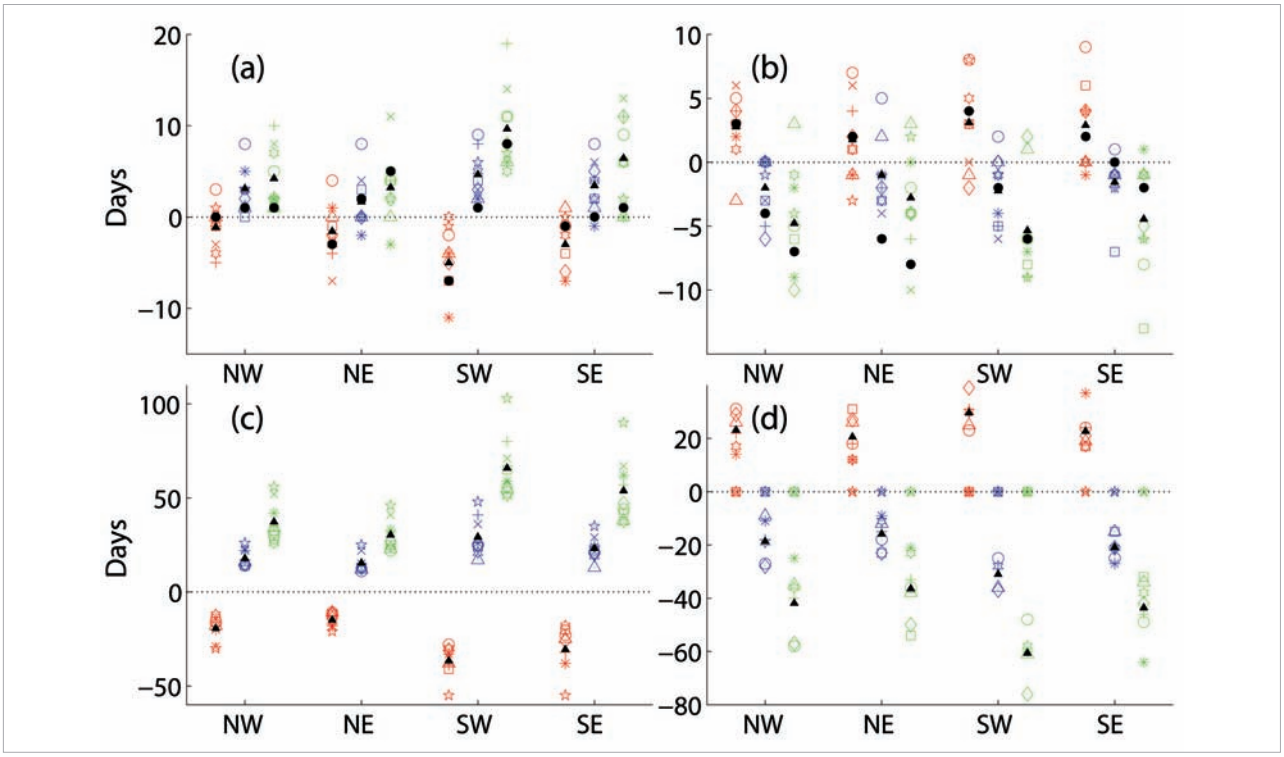

Figure 22b. Changes in beginning dates (red), end dates (blue), and lengths (green) of local (a) summer/(b) winter between Period II and Period I in the 20c3m experiments; (c)/(d) are the same as (a)/(b) except for the doubling-to-quadrupling-CO_2 experiments. A positive value indicates delay of date or increase in length, while a negative value indicates an earlier date or decrease in length. The marks represent different models, ensemble mean, and observation as same as in Figure 22a. Units: number of days.

Reference:

Xia, J. J., Z. W. Yan and W. Zhou, 2011: Changes in seasonality in China under enhanced atmospheric CO_2 concentration. *Atmospheric and Oceanic Science Letters*, **4(1)**, 12-17.

4. Climatic Impact of Modern Volcanic Eruptions

(PI: Wyss YIM)

The influence of volcanic eruptions on regional and global precipitation variability is poorly understood in comparison to temperature. This project is aimed at studying the climatic impact of 'modern' volcanic eruptions since Krakatau, Indonesia in 1883 through an examination of the instrumental observation record and available information including satellite images and weather reports.

The main objective of this project is to study the climatic impact of 'major' modern volcanic eruptions since 1883 using temperature and rainfall records of the Hong Kong Observatory (formerly Royal Observatory Hong Kong) and other information. 'Major' is defined by the Volcanic Explosivity Index (VEI) of Newhall and Self (1982) as having reached the scale of 4 and above.

'Major' volcanic eruptions are found to decrease the earth's surface air temperature because of the tephra and gases released into the atmosphere (Yim, Huang and Chan, to be submitted). In spite of the pronounced urban heat island effect (UHI) on the temperature record of the Hong Kong Station, lower annual mean temperatures in subsequent years than during the eruption year can be found in the majority of the eruptions investigated. Other important conclusions drawn include:

(1) 1884 with the lowest mean annual temperature of 21.4°C is best explained by cooling following the 1883 eruption of Krakatau.
(2) A correction for UHI for the temperature record of the Hong Kong Station is essential for studying climate change.
(3) Lowering of annual mean temperatures of the Hong Kong Station lasting at least several years have occurred after 'major' eruptions. Notable examples include Krakatau, Indonesia in 1883, Santa Maria, Guatemala in 1902 and Kharimkotan, USSR in 1933.

Volcanic eruptions have been found to be a cause of East Asian monsoonal precipitation variability (Yim and Chan 2009; Yim 2010a). Both abnormally dry and wet years can be the end result but dry years are more common than wet years. This difference can be explained by the redistribution of water vapour within the atmosphere caused by the volcanic eruptions. Examples of abnormally dry years include the driest year since record began with 901.1 mm total rainfall in 1963 during the Agung eruption in Indonesia and the tenth driest year since record began with 1639.1 mm annual rainfall in 1991 during the Pinatubo eruption in Philippines. Abnormally wet years include the second wettest year since record began with 3247.5 mm total rainfall in 1982 during the El Chichón eruption in Mexico and the sixth wettest year since record began with 3066.2 mm total rainfall during the Chaitén eruption in Chile in 2008. As a consequence of the coastal flooding during the June 7, 2008 rainstorm in Hong Kong (Yim 2010b) preventive works to reduce flood risks are in progress by the Drainage Services Department of the Hong Kong SAR Government.

References:

Newhall, C. G. and S. Self, 1982: The volcanic explosivity Index (VEI): An estimate of explosive magnitude of historic volcanism. *Journal of Geophysical Research*, **87**, 1231-1238.

Yim, W. W.-S., 2010a: A role for 'major' volcanic eruptions in monsoonal precipitation variability. Geophysical Research Abstracts, **12**, EGU2010-8390-1.

Yim, W. W.-S., 2010b: Extreme regional precipitation events related to volcanic eruptions. European Science Foundation – COST High Level Research Conference on Extreme environmental events, Cambridge, UK.

Yim, W. W.-S. and J. C. L. Chan, 2009: Volcanic forcing of monsoonal precipitation variability in selected modern eruptions. American Geophysical Union Fall Meeting, abstract NH33B-1147.

F. Air Quality and Climate

1. Identifying Source and Patterns of Nitrogen Oxide Pollutants for Air Quality Predictions
(PI: Mark WENIG)

This project measures NO_2 concentrations in the air in order to identify emission patterns and source terms, which is essential for determining the anthropogenic impact on the urban environment and climate.

In this project, we did a measurement campaign using a cavity enhanced DOAS (differential optical absorption spectroscopy) instrument to measure the nitrogen oxide distribution in Hong Kong. This new type of instrument has been developed recently at Heidelberg University, Germany. This new technology allows very precise measurements of pollutants and the instrument is small enough that it can be carried around in a car.

Two scientists from Heidelberg University visited CityU in December 2010 within the framework of a Germany/HK Joint Research Scheme project that the PI has with Heidelberg University, and they brought a cavity enhanced DOAS instrument with them. We rented a van so that we could drive the instrument around and covered almost every part of Hong Kong. The instrument measures the NO_2 concentration every 2s and

we measured for 8 days, 13 hours per day, so we have a very large and high resolution data set. We are currently working on processing the data and combining the street measurements with the long-path DOAS instrument which is installed at the roof top at CityU. This instrument is measuring over a very long light path using a retro reflector which we installed in Mong Kok in December 2010. A first comparison of the measurement data can be seen in Figure 23. The EPD data are higher since they are closer to street level, especially the Mong Kok measurement station, but the correlation is very good. This data will be used to remove city-wide temporal variations in order to focus on the spatial emission patterns.

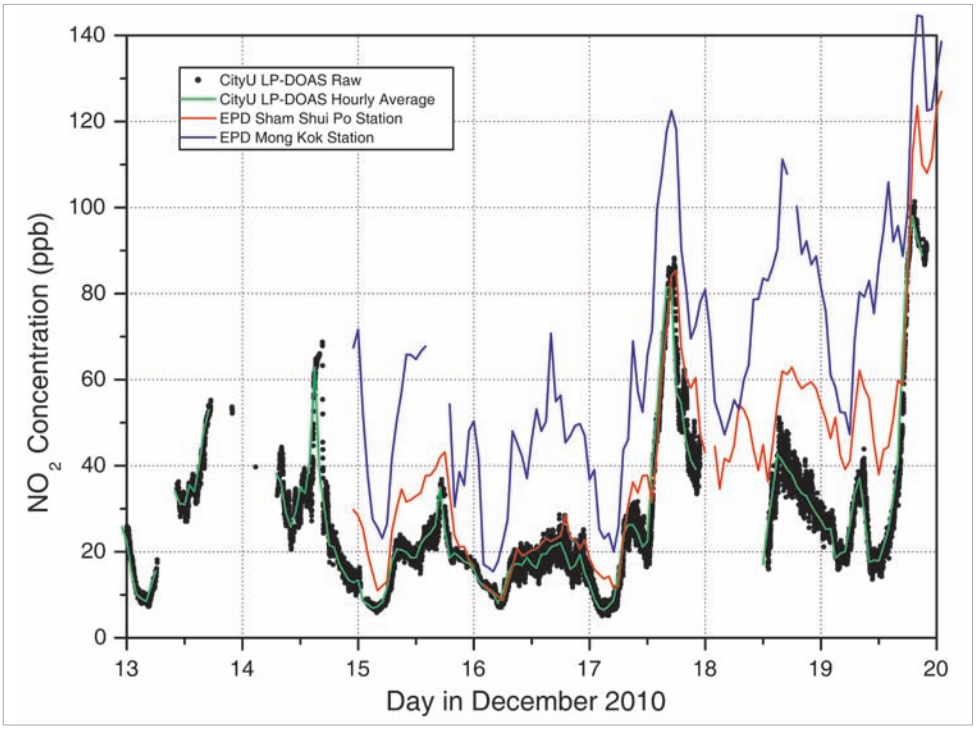

Figure 23. Comparison of the CityU LP-DOAS NO_2 measurement results with the EPD data from the Sham Shui Po and the Mong Kok measurement station.

2. Analyzing the Probability of Dust Events in Hong Kong Caused by Transported Desert Dust and Their Impact on Local Air Quality

(PI: Mark WENIG)

Even though Hong Kong is not located close to a desert, local air quality can be affected by transported desert dust if certain meteorological conditions are met. In this project we investigate the long range transport of dust originating from different deserts and identified the sources and their contribution to air pollution levels in Hong Kong.

In this study, we used aluminium (Al) and calcium (Ca) concentration measurements in Hong Kong, as well as NASA's daily aerosol index images (TOMS and OMI) air parcel backward trajectories to Hong Kong using the NOAA HYSPLIT model to study and identify dust sources impacting Hong Kong. We found out that the mean Ca/Al mass ratios of sources involving the Taklamakan desert are notably higher than those for non-East Asian sources owing to a higher Ca content of most of the East Asian deserts. Contributions from the desert sources are estimated using the average Al abundance of 8% in the upper continental crust to convert the Al mass in the PM_{10} to dust concentrations for the dust events identified with air mass purely of non-East Asian origin. Results reveal that the average contribution from the non-East Asian sources is approximately 10% and that from the Thar, the Arabian and the Sahara deserts is about 8% each.

Afterwards, we focused on two dust episodes in Hong Kong, one occurring in March 2006 and the other on 22 March 2010. The latter is the worst dust episode on Hong Kong record. We determined that the 16 March 2006 episode is traceable to a continental scale Saharan dust outbreak of 5-9 March 2006 caused by the cold front of an East Mediterranean Sharav cyclone arriving at North-west Africa on 5 March 2006. We used chemical transport simulations using the GOCART (Goddard Chemistry Aerosol Radiation and Transport) model to track the movements of desert dust. This provided a visible evidence of the transport as well as an estimate of contributions from the Sahara to the aerosol concentration levels in Hong Kong.

Figure 24 shows the agreement of dust transport simulation results derived using the GOCART model with the aerosol index from the Ozone Monitoring Instrument (OMI).

The major source of dust for Hong Kong is usually the Gobi desert. Despite the effect of remote sources, the 16 March 2006 dust episode was still mainly under the influence of the Mongolian cyclone / cold front. In the recent episode of 22 March 2010, the influence of the Mongolian cyclone predominated as well. It appears that the concurrent influence of the Sharav and Mongolian cyclones on Hong Kong and East Asia is not a common occurrence.

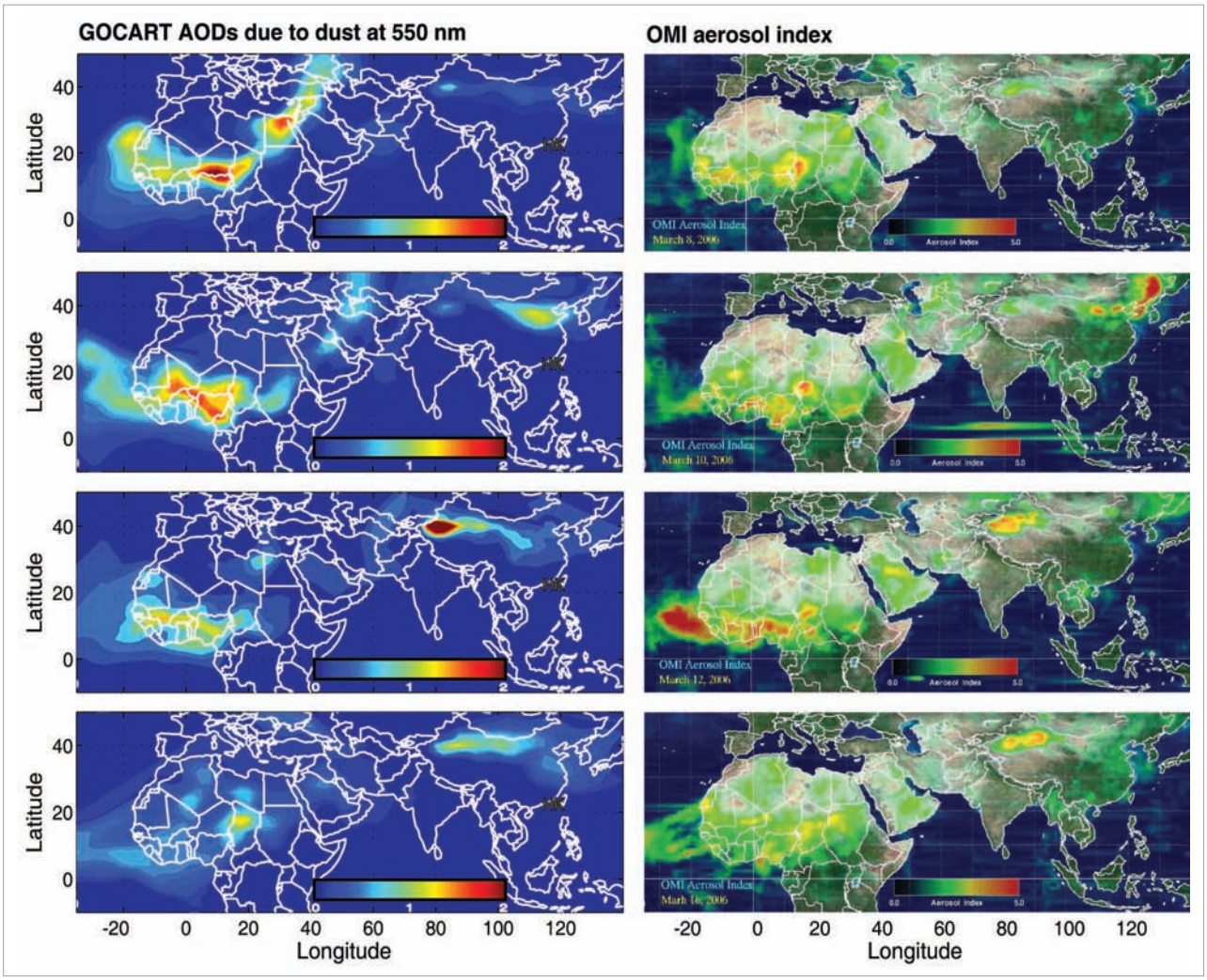

Figure 24. Comparison of dust transport simulation results from the Goddard Chemistry Aerosol Radiation and Transport (GOCART) model with the aerosol index from the Ozone Monitoring Instrument (OMI).

3. Analysis of the Correlation between Global Warming and Increasing Trends of Ozone and other Trace Gases

(PI: Mark WENIG)

The effects of global warming are numerous ranging from sea level rise to changes of the weather system. This project analyzes the impact global warming can have on pollution levels like ozone and other trace gas concentrations which can influence public health.

In this project we investigated the effects of temperature rise, which could be due to global warming, on air pollutants in Hong Kong at three monitoring sites, with regard to their sensitivity to global warming and the pollutant trends observed over the period of 1990's to 2009. At the measurement site in Sha Tin which generally records higher ozone levels, an upward trend is clearly evident in the statistical tests. Results of correlation coefficients and regression slopes (95% confidence) over the period of 1997-2009 showing a gradual increase in sensitivity of ozone to temperature rise though the highly urbanized site in Tsuen Wan is much less sensitive. Regarding isoprene, statistical tests also yields a positive trend for summer. However, the data for isoprene are inadequate owing to fewer samples since 2004.

An increasing trend is clearly observed in mean ozone concentrations at all three monitoring sites and for all seasons. The increase is prominently the most significant in autumn, ranging from 1.07 μg m^{-3} to 1.79 μg m^{-3} per year, and remarkably the lowest in summer at all sites. This ozone trend in Hong Kong seems to be consistent with the recent trend (2006-09) of the Pearl River Delta region. Despite a show of significant sensitivity to temperature change in summer, only a slight upward trend is observed in summer isoprene concentrations. Besides ozone and summer isoprene, sulphate was rising from 1996 to 2007, but declines in 2008 and 2009.

Interactions exist between isoprene, ozone and sulphate. Isoprene correlates significantly with filtered maximum ozone (r=0.72), suggesting a role of isoprene in elevated ozone levels. Increase in both, ozone and moisture, result in abundant OH radicals, and indirectly more H_2O_2, both of which convert sulphur to sulphate. For this reason, non sea-salt sulphate correlates significantly with maximum ozone (not filtered, r=0.65).

G. Air-Sea Interaction Studies

1. Teleconnected Influence of North Atlantic Sea Surface Temperature on the El Niño Onset

(PI: Wen ZHOU)

The SST-induced heating over the North Atlantic produces an East Atlantic/West Russia teleconnected pattern, then strengthens the East-Asian winter monsoon, and further help initiate a Pacific El Niño event.

Influence of North Atlantic sea surface temperature (SST) anomalies on tropical Pacific SST anomalies is examined in this study (Figure 26). Both summer and winter North Atlantic SST anomalies are negatively related to central-eastern tropical Pacific SSTa in the subsequent months varying from 5 to 13 months. In particular, when the North Atlantic is colder than normal in the summer, an El Niño event is likely to be initiated in the subsequent spring in the tropical Pacific. A mechanism is suggested in Figure 25. Associated with summer cold North Atlantic SST anomalies is an anomalous cyclonic circulation at low-level over the North Atlantic from subsequent October to April. Corresponded to this local response, an SST-induced heating over the North Atlantic produces a teleconnected pattern, similar to the East Atlantic/West Russia (EA/WR) teleconnection. The pattern features two anticyclonic circulations near UK and Lake Baikal, and two cyclonic circulations over the North Atlantic and near the Caspian Sea. The anticyclonic circulation near Lake Baikal enhances the continental northerlies, and strengthens the East-Asian winter monsoon. These are

also associated with an off-equatorial cyclonic circulation in the western Pacific during the subsequent winter and spring, which produces equatorial westerly wind anomalies in the western Pacific. The equatorial westerly wind anomalies in the winter and spring can help initiate a Pacific El Niño event following a cold North Atlantic in the summer. More detailed information refer to Wang et al. (2010).

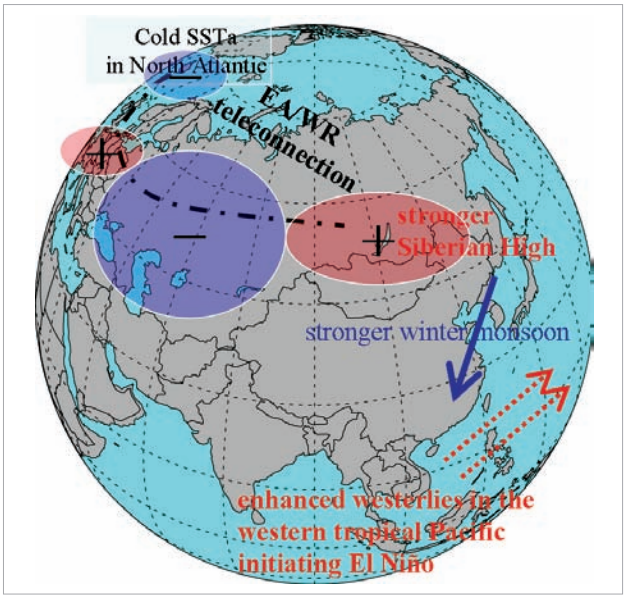

Figure 25. Schematic illustration of how the summer North Atlantic SSTa impacts on El Niño onset in next year.

Reference:

Wang, X., C. Z. Wang, W. Zhou, D. X. Wang and J. Song, 2010: Teleconnected influence of North Atlantic Sea surface temperature on the El Niño onset. *Clim. Dyn.*, DOI: 10.1007/s00382-010-0833-z.

2. Interannual Heat Content Variability in the South China Sea and Its Response to ENSO

(PI: Wen ZHOU)

The effects of wind stress curl and latent heat flux, combined with the westward propagating negative (positive) ocean heat content anomalies from the western Pacific, may contribute to rapid growth and propagation of the ocean heat content anomalies in the northern South China Sea.

The interannual variability of upper ocean heat content (OHC) in the South China Sea (SCS) for the period of 1987 to 2006 and its response to ENSO events are investigated (Figure 26). It is found that the variability has a good correspondence with ENSO events, but with opposite phase. Negative OHC anomalies appear during ENSO warm phases, while positive OHC anomalies occur during ENSO cool phases. In addition, negative (positive) OHC anomalies propagate westward obviously during ENSO warm (cool) phases in the northern SCS. In contrast, OHC anomalies in the southern SCS do not exhibit distinct westward propagation during ENSO events. To explore why the OHC anomalies cannot propagate westward in the southern SCS, the interannual variability of oceanic and atmospheric anomaly fields including wind stress curl (WSC), horizontal wind stress, latent heat flux (LHF) and sea level pressure (SLP) are investigated. The results show that after a mature phase of ENSO warm (cool) event, negative (positive) OHC anomalies first appear in the northern SCS, which comes from the western Pacific through Luzon Strait. Then cyclonic (anticyclonic) wind stress anomalies occur in the northern SCS, which leads to positive (negative) WSC anomalies. Meanwhile, positive (negative) LHF anomalies which correspond to oceanic heat loss (gain) occur in this region. The effects of WSC and LHF, combined with the westward propagating negative (positive) OHC anomalies from the western Pacific, may contribute to rapid growth and propagation of the OHC anomalies in the northern SCS. On the contrary, the negative (positive) WSC and LHF anomalies associated with positive (negative) SLP in the southern SCS seem to be the important processes responsible for the weakening and non-propagation of the OHC anomalies in the southern SCS after a mature phase of ENSO warm (cool) event. More detailed information refer to Yan et al. (2010).

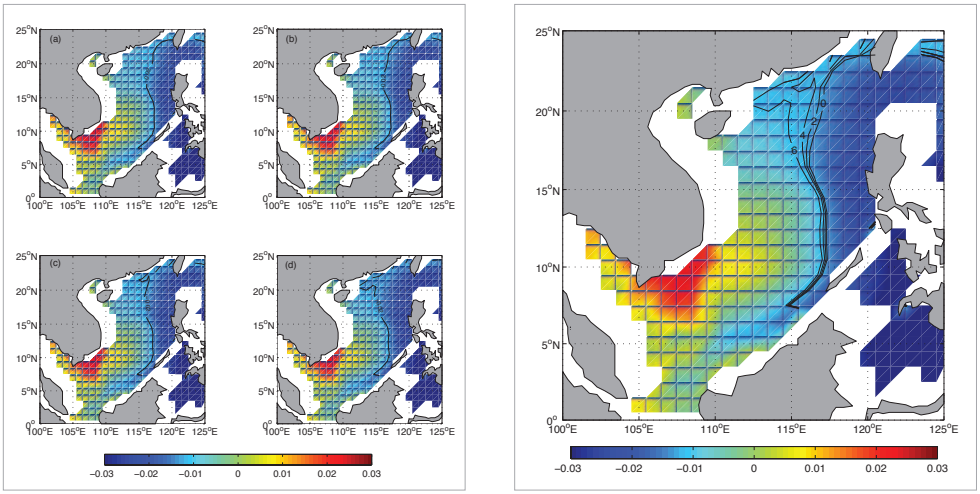

Figure 26. Left panel: the temporal-spatial evolution of the first EEOF mode (EEOF1) in the SCS. The spatial patterns are displayed at an interval of every 2 months with a sequence of (a) for 0, (b) for 2, (c) for 4, and (d) for 6 months. The contour line of -0.02 with time 0, 2, 4 and 6 months is also depicted for easy viewing. Right panel: Same as Left panel but for the temporal evolution of contour line -0.02 at 0, 2, 4 and 6 months.

Reference:

Yan, Y. F., Y. Q. Qi and W. Zhou, 2010: International heat content variability in the South China Sea and its response to ENSO. *Dynamics of Atmospheres and Oceans*, **50**, 400-414. Doi: 10.1016/j.dynatmoce.2010.07.002.

H. Paleoclimate Studies

1. Aspects of Quaternary Environmental Change in the Pearl River Mouth Region

(PI: Wyss YIM)

This is long-term project on the reconstruction of environmental change over the past 0.5 million years supported by competitive research grants provided by the Research Grants Council of the Hong Kong SAR Government.

The research work has been in three areas:

(1) Salinity changes including the use of diatoms as indicators (Zong et al. 2010b; Zong et al. 2010c).
(2) Carbon cycling in estuarine sediments (Yu et al. 2010; Yang et al. 2011)
(3) Sedimentary evidence of Late Holocene human activity (Zong et al. 2010a)

References:

Yang, S, M. Tang, W. W.-S. Yim, Y. Zong, G. Huang, A. D. Switzer and Y. Saito, 2011: Burial of organic carbon in Holocene sediments of the Zhujiang (Pearl River) and Changjiang (Yangtze River) estuaries. *Marine Chemistry*, **123**, 1-10.

Yu, F., Y. Zong, J. M. Lloyd, G. Huang, M. J. Leng, C. Kendrick, A. L. Lamb and W. W.-S. Yim, 2010: Bulk organic $\delta^{13}C$ and C/N as indicators for sediment sources in the Pearl River delta and estuary, southern China. *Estuarine Coastal and Shelf Science*, **87**, 618-630.

Zong, Y., A. C. Kemp, F. Yu, J. M. Lloyd, G. Huang and W. W.-S. Yim, 2010a: Diatoms from the Pearl River estuary, China and their suitability as water salinity indicators for coastal environments. *Marine Micropaleontology*, **75**, 38-49.

Zong, Y., F. Yu, G. Huang, J. M. Lloyd and W. W.-S. Yim, 2010b: The history of water salinity in the Pearl River estuary, China, during the Late Quaternary. *Earth Surface Processes and Landforms*, **35**, 1221-1233.

Zong, Y., F. Yu, J. M. Lloyd and W. W.-S. Yim, 2010c: Sedimentary evidence of late Holocene human activity in the Pearl River delta, China. *Earth Surface Processes and Landforms*. **35**, 1095-1102.

Publications

Journal Papers

Chand, Savin S., Kevin J. E. Walsh and J. C. L. Chan, 2010: A Bayesian Regression Approach to Seasonal Prediction of Tropical Cyclones Affecting the Fiji Region. *Journal of Climate*, **23**, 3425-3445.

Chow, K. C. and J. C. L. Chan, 2010: A dual-scheme approach of cumulus parameterization for simulating the Asian summer monsoon. *Meteor. Appl.*, **17**, 287-297.

Feng, J., W. Chen, C.-Y. Tam and W. Zhou, 2010: Different Impacts of El Niño and El Niño Modoki on China Rainfall in the Decaying Phases. *Int'l J. Climatol.*, DOI: 10.1002/joc.2217.

Huang, J., X. Wang, W. Zhou, D. Wang and F. Zhou, 2010: The Characteristics of Sea Fog with Different Airflow over the Yellow Sea in Boreal Spring. *Acta Oceanol. Sin.*, **29**, 3-12.

Huang, W.-R., S-Y Wang and J. C. L. Chan, 2010: Discrepancies between global reanalyses and observations in the interdecadal variations of Southeast Asian cold surge. *International Journal of Climatology*, DOI: 10.1002/joc.2234.

Huang, W.-R., J. C. L. Chan and S. Y. Wang, 2010: A planetary-scale land–sea breeze circulation in East Asia and the western North Pacific. *Quarterly Journal of the Royal Meteorological Society*, **136**, 1543-1553.

Knutson, T. R., J. L. McBride, J. C. L. Chan, K. Emanuel, G. Holland, C. Landsea, I. Held, J. P. Kossin, A. K. Srivastava and M. Sugi, 2010: Tropical cyclones and climate change. *Nature Geoscience*, **3**, 157-163.

Lee, Y. C., X. Yang and M. Wenig, 2010: Transport of Dusts from East Asian and non East Asian Sources to Hong Kong during Dust Storm Related Episodes/Events 1996-2007. *Atmospheric Environment*, **44**, 3728-3738.

Liu, K. S. and J. C. L. Chan, 2010: Interannual variation of Southern Hemisphere tropical cyclone activity and seasonal forecast of tropical cyclone number in the Australian region. *Int'l J. Climatology*, DOI: 10.1002/joc.2259.

Liu, Q. Y. and Zhou W, 2010: The relationship between the Northwestern Pacific Typhoon Activity and the Upper-ocean Heat Content at Interdecadal Time Scale. *Journal of Tropical Oceanography*, **29**, 8-14.

Wang, D. X., W. Zhou, X. L. Yu, Q. Xie and X. Wang, 2010: Marine Atmospheric Boundary Layers Associated with Summer Monsoon Onset over the South China Sea in 1998. *Atmospheric and Oceanic Science letters*, **3**, 263-270.

Wang, W. W., Y. Q. Yu, C. Li, W. Zhou, Q. Y. Liu and D. X. Wang, 2010: An Investigation of the South China Sea Throughflow and Its Impact on Upper Layer Heat Content of the South China Sea using LICOM. *Acta Oceanologica Sinica*, **32(2)**, 1-11.

Wang, X., C. Z. Wang, W. Zhou, D. X. Wang and J. Song, 2010: Teleconnected Influence of North Atlantic Sea Surface Temperature on the El Niño Onset. *Clim. Dyn.*, DOI:10.1007/s00382-010-0833-z.

Wu, Q. Z., Z. Wang, A. Gbaguidi, X. Tang and W. Zhou, 2010: Numerical Study of The Effect of Traffic Restriction on Air Quality in Beijing. *Scientific Online Letters on the Atmosphere*, **6A**, 17–20, doi:10.2151/sola.6A-005.

Yu, F., Y. Zong, J. M. Lloyd, G. Huang, M. J. Leng, C. Kendrick, A. L. Lamb and W. W.-S. Yim, 2010: Bulk organic $\delta^{13}C$ and C/N as indicators for sediment sources in the Pearl River delta and estuary, southern China. *Estuarine, Coastal and Shelf Science*, **87**, 618-630.

Publications

Research Briefs

2010 Predictions of Seasonal Tropical Cyclone Activity over the Western North Pacific

Forecasts of the number of tropical cyclones making landfall in (1) South China and (2) the Korea-Japan region in 2010

Verification of Forecasts of Tropical Cyclone Activity in the Australian region in 2009/10

Updated Prediction of Seasonal Tropical Cyclone Activity over the Western North Pacific for 2010

Updated forecasts of the number of tropical cyclones making landfall in (1) South China and (2) the Korea-Japan region in 2010

2010/11 Predictions of Seasonal Tropical Cyclone Activity in the Australian Region

Staff list

Director

Prof. Johnny CHAN	Dean, School of Energy and Environment Chair Professor of Atmospheric Science

Members

Prof. Ronghui HUANG	Honorary Professor (Academician, Chinese Academy of Sciences)
Prof. Chongyin LI	Honorary Professor (Academician, Chinese Academy of Sciences)
Dr. Francis TAM	Assistant Professor
Dr. Mark WENIG	Assistant Professor
Dr. Wen ZHOU	Assistant Professor

Advisory Committee

Prof. Yihui DING	Academician, Chinese Academy of Engineering
Lord Prof. Julian HUNT	Professor, University College London, Fellow of Royal Society

Researchers

Appointed by Centre

Prof. Wyss W.-S. YIM	Senior Research Fellow
Dr. HUANG Wan-ru	Research Fellow
Dr. LEE Yuk Chun	Research Fellow
Mr. LIU Kin Sik	Senior Research Assistant
Miss AU-YEUNG Yee Man	Research Assistant
Mr. CHIU Kwok Shing	Research Assistant
Mr. FUNG Ka Yu	Research Assistant
Mr. NG Ka Wai	Research Assistant

Visiting from other institutions

Dr. LIU Qinyan	South China Sea Institute of Oceanology Chinese Academy of Sciences
Ms. MA Yin	Center for Monsoon System Research, Institute of Atmospheric Physics, Chinese Academy of Sciences

Guy Carpenter Asia-Pacific Climate Impact Centre
City University of Hong Kong
Tat Chee Avenue, Kowloon,
Hong Kong, China.

Tel: (852) 3442 7359
Email: gcacic@cityu.edu.hk
Website: http://www.cityu.edu.hk/gcacic/

MIX
Paper from responsible sources
FSC™ C006398
www.fsc.org

Printed with SOY INK